Geophysical Journal International

Geophys. J. Int. (2013) **193,** 61–77 doi: 10.1093/gji/ggs129

Interseismic GPS strain data inversion to estimate slip-deficit rates at plate interfaces: application to the Kanto region, central Japan

Akemi Noda,[1] Chihiro Hashimoto,[2] Yukitoshi Fukahata[3] and Mitsuhiro Matsu'ura[4]

[1] *Kozo Keikaku Engineering Inc., Nakano-ku, Tokyo* 164–0012*, Japan. E-mail: akemi-noda@kke.co.jp*
[2] *Graduate School of Environmental Studies, Nagoya University, Nagoya* 464–8601*, Japan*
[3] *Disaster Prevention Institute, Kyoto University, Uji, Kyoto* 611–0011*, Japan*
[4] *Institute of Statistical Mathematics, Tachikawa, Tokyo* 190–8562*, Japan*

Accepted 2012 December 30. Received 2012 December 14; in original form 2012 July 28

SUMMARY

We developed an inversion method to estimate unbiased interseismic slip-deficit rates at plate interfaces from observed GPS velocity data with an elastic dislocation model. In this method, first, we subtract theoretical surface velocities due to known steady relative plate motion from the observed GPS data, and presume the residuals to be caused by slip deficit at plate interfaces. However, the observed GPS data always include rigid block translation and rotation, which cannot be explained by the elastic dislocation model. We treated the rigid block translation and rotation as systematic errors in the analysis, and removed them by transforming the velocity data into the average strain rates of triangle elements composed of adjacent GPS stations. By this transformation, original information about intrinsic deformation is preserved. Applying a unified Bayesian inversion formula to the GPS strain data, we can obtain unbiased slip-deficit rate distribution. We demonstrated the applicability of the method of GPS strain data inversion through the analysis of interseismic GPS velocity data (1996–2000) in the Kanto region, central Japan, where the North American (NAM), Pacific (PAC) and Philippine Sea (PHS) plates are interacting with each other in a complicated way. From this analysis we found a broad and high slip-deficit rate zone on the NAM-PHS plate interface, extending from southeast off the Boso peninsula to the Tokai region through the Izu-Mainland collision zone. Two high slip-deficit rate zones along the Sagami and Suruga troughs correspond to the source regions of the 1923 Kanto earthquake (M7.9) and a potential Tokai earthquake. On the PHS-PAC plate interface, though the estimation errors are large, we found a moderate slip-deficit rate zone far southeast off the Boso peninsula, where an M7.4 earthquake has occurred in 1953.

Key words: Inverse theory; Space geodetic surveys; Plate motions; Subduction zone processes; Kinematics of crustal and mantle deformation.

1 INTRODUCTION

The occurrence of earthquakes can be regarded as the release of tectonically accumulated stress by sudden faulting (Knopoff 1958; Savage 1969). In the case of interplate earthquakes, the stress accumulation results from interseismic slip deficit (back slip) at plate interfaces (Savage & Prescott 1978; Spence & Turcotte 1979). Surface deformation due to slip deficit can be computed on the basis of elastic dislocation theory. Then, we can formulate the inverse problem of estimating unknown slip-deficit rates at plate interfaces from observed surface deformation data. On the concept of back slip, for example, Matsu'ura *et al.* (1986) modelled the San Andreas–Sargent–Calaveras fault system, California, by segmented steadily slipping block boundaries with shallow partially locked portions (seismogenic faults), and estimated the steady-slip rates of block boundaries and the slip rates and widths of seismogenic faults by applying an inversion formula for Bayesian models incorporating direct prior information about the values of model parameters (Jackson & Matsu'ura 1985) to trilateration data of the Hollister network spanning the fault system. In this analysis, the differences of fault-slip rates from block-slip rates give the slip-deficit rates.

In the Jackson–Matsu'ura inversion formula, relative weight of prior information to observed data is fixed in advance, and so it gives a maximum likelihood solution. To optimize the relative weight, that is, to select the best among possible maximum likelihood solutions, Yabuki & Matsu'ura (1992) introduced Akaike's Bayesian Information Criterion (ABIC; Akaike 1980) based on the entropy maximization principle (Akaike 1977), and developed an inversion method to estimate coseismic fault-slip distribution from geodetic data by incorporating indirect prior information about the spatial variations of model parameters. Yoshioka *et al.* (1993, 1994) have applied the Yabuki–Matsu'ura inversion method to interseismic

levelling and trilateration data, and estimated the spatial distribution of slip-deficit rates at plate interfaces in the Tokai and Kanto regions, central Japan, assuming the concept of back slip to be applicable. However, in the case of convergent plate boundaries, the concept of back slip is not applicable unlike the case of transcurrent plate boundaries, because steady plate subduction inevitably causes intrinsic crustal deformation (Matsu'ura & Sato 1989; Sato & Matsu'ura 1992; Hashimoto *et al.* 2004).

Since daily station-coordinate data of GEONET (a nation-wide dense GPS network in Japan) became available, a number of attempts to estimate interseismic slip-deficit rates at plate interfaces in the Japan region from GPS displacement rate (velocity) data have been done with the Yabuki–Matsu'ua inversion method (e.g. Sagiya 1999, 2004; Ito *et al.* 1999, 2000; Nishimura *et al.* 2004; Suwa *et al.* 2006) but without considering the effects of steady plate subduction. In the analysis of GPS displacement data, unlike trilateration data, another serious problem arises, because the displacement data include rigid block translation and rotation. The Earth's crust is usually treated as a linear elastic body, but it includes a number of defects such as micro cracks and active faults spreading over tectonic boundary zones. Interseismic brittle fracture and/or plastic flow at these defects cause some rigid translation and rotation of crustal blocks, which cannot be explained by simple slip-deficit models based on elastic dislocation theory (Noda & Matsu'ura 2010). If observed data contain theoretically unexplainable coherent noise (systematic errors), the result of inversion analysis will be seriously biased.

One of the effective ways to remove rigid block translation and rotation from GPS array data is to transform observed horizontal displacement vectors into changes in distance between adjacent GPS stations, which correspond to baseline length changes in trilateration. To avoid the dependence of horizontal displacement vectors on the choice of a fixed point, Ito *et al.* (1999, 2000) have used the baseline length changes transformed from GPS displacement data in the estimation of interplate slip-deficit rates in southwest and northeast Japan. Hashimoto *et al.* (2009, 2012) have also used the baseline length changes but to remove the systematic errors due to rigid block translation and rotation from GPS array data. Applying an inversion formula for Bayesian models incorporating both direct and indirect prior information (Matsu'ura *et al.* 2007) to the baseline length change data, they succeeded in obtaining unbiased slip-deficit rate distribution on the North American–Pacific plate interface in northeast Japan. Noda & Matsu'ura (2010) have given a theoretical basis for the use of baseline length changes instead of horizontal displacement data.

A similar but more direct way to remove rigid block translation and rotation from GPS array data is to transform observed horizontal displacement vectors into average strain tensors for individual triangles composed of adjacent GPS stations (Appendix). This transformation is linear, and so original information in GPS array data is preserved without distortion. Mazzotti *et al.* (2000) and Henry *et al.* (2001) have pointed out the advantage of using strain tensors instead of displacement vectors in the inversion analysis of GPS array data to estimate the interseismic locking depths and coupling ratios of plate interfaces in the Japan region. However, their strain tensors are not the average strain tensors of individual triangles but the weighted local averages of them defined at GPS stations. In their cases, the transformation of displacement vectors into strain tensors is not linear, and so original information in GPS array data will be distorted.

In Section 2 of this paper, taking all the points mentioned above into consideration, we develop an inversion method to estimate unbiased distribution of interseismic slip-deficit rates at plate interfaces from GPS array data. In Section 3, we demonstrate the applicability of the inversion method through the analysis of interseismic GPS array data (1996–2000) in the Kanto region, central Japan.

2 MATHEMATICAL FORMULATION

In this section, we mathematically formulate the inverse problem of estimating interseismic slip-deficit rates at plate interfaces from GPS array data on the basis of Bayesian statistical inference theory. First, we derive expressions for interseismic surface velocities due to the increase of slip deficit at plate interfaces by applying the technique of hereditary integral to general solutions for a step-type point dislocation source. Second, parameterizing slip-deficit rate distribution with known basis functions, we obtain a vector-form observation equation for GPS velocity data. Third, we transform the observation equation for velocity data into that for strain rates. Finally, incorporating direct and indirect prior information into observed data, we construct a Bayesian model with hierarchic structure controlled by hyperparameters, for which Matsu'ura *et al.* (2007) give an inversion formula to obtain optimum solution.

2.1 Representation of interseismic crustal deformation

We consider an elastic surface layer overlying Maxwell-type viscoelastic half-space under gravity, and take a Cartesian coordinate system (x_1, x_2, x_3) so that the x_1–x_2 plane coincides with the free surface and the x_3-axis points vertically upwards as shown in Fig. 1. The elastic surface layer corresponds to the lithosphere, and the viscoelastic half-space to the asthenosphere. We introduce an interface $\Sigma(\boldsymbol{\eta})$ that divides the elastic surface layer into two plates. Given the 3-D geometry of the plate interface in a functional form,

$$x_3 = f(x_1, x_2), \tag{1}$$

we can compute the unit normal vector $\mathbf{n}$ of $\Sigma(\boldsymbol{\eta})$ as

$$\mathbf{n} = \begin{pmatrix} n_1 \\ n_2 \\ n_3 \end{pmatrix} = \frac{1}{\sqrt{(\partial_1 f)^2 + (\partial_2 f)^2 + 1}} \begin{pmatrix} -\partial_1 f \\ -\partial_2 f \\ 1 \end{pmatrix}. \tag{2}$$

Here, $\partial_{1(2)}$ denotes partial differentiation with respect to the spatial coordinate x_1 or x_2.

By definition, any indigenous source in an elastic body can be represented by a moment tensor (Backus & Mulcahy 1976a,b). We suppose that the elastic body has been in an equilibrium state under

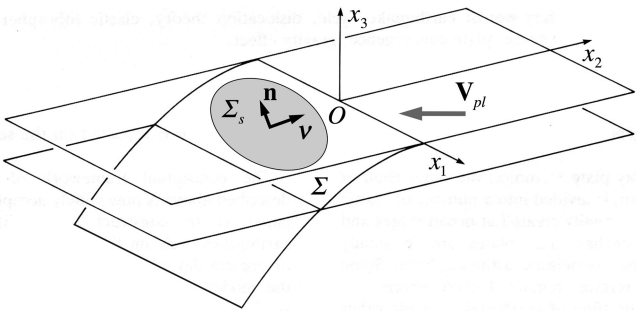

Figure 1. A coordinate system, plate interface geometry, and the notation of normal and slip-direction vectors. The shaded portion of the plate interface Σ represents a potential seismogenic region Σ_s. The black arrows, $\mathbf{n}$ and $\boldsymbol{\nu}$, denote the unit normal and slip-direction vectors, respectively. The grey arrow shows the horizontal motion of the underlying plate relative to the overlying plate.

gravity before the time $t = 0$. Then, for given moment density tensor distribution $m_{pq}(\boldsymbol{\xi}, t)$ in a source region V_s, the quasi-static displacement field $u_i(\mathbf{x}, t)$ is expressed in the form of convolution integral:

$$u_i(\mathbf{x}, t) = \int_0^t dt' \int_{V_s} \partial_q G_{ip}(\mathbf{x}, t - t'; \boldsymbol{\xi}, 0)\, \dot{m}_{pq}(\boldsymbol{\xi}, t')\, d\boldsymbol{\xi} \quad t \geq 0. \tag{3}$$

Here, $G_{ip}(\mathbf{x}, t; \boldsymbol{\xi}, t')$ represent the quasi-static displacement responses at a point $\mathbf{x}$ and time t to unit step-type single force at a point $\boldsymbol{\xi}$ and time t', $\partial_q G_{ip}(\mathbf{x}, t; \boldsymbol{\xi}, t')$ are their partial derivatives with respect to ξ_q, and the dot means differentiation with respect to t. The explicit expressions of the partial derivatives of displacement response functions are given in Yabuki & Matsu'ura (1992) for an elastic half-space model and Hashima *et al.* (2008) for an elastic-viscoelastic layered half-space model with gravitational effects.

When the distribution of moment density tensor is localized at a plate interface $\Sigma(\boldsymbol{\eta})$, using the Dirac delta function $\delta(\boldsymbol{\xi} - \boldsymbol{\eta})$, we can represent it as

$$m_{pq}(\boldsymbol{\xi}, t) = m^{\Sigma}_{pq}(\boldsymbol{\eta}, t)\delta(\boldsymbol{\xi} - \boldsymbol{\eta}). \tag{4}$$

In the case of fault slip, the explicit expression of m^{Σ}_{pq} is given by

$$m^{\Sigma}_{pq}(\boldsymbol{\eta}, t) = \mu w(\boldsymbol{\eta}, t)[\nu_p(\boldsymbol{\eta}) n_q(\boldsymbol{\eta}) + \nu_q(\boldsymbol{\eta}) n_p(\boldsymbol{\eta})], \tag{5}$$

where μ is the rigidity of the elastic medium surrounding the source, w the magnitude of fault slip, $\boldsymbol{\nu}$ the unit slip-direction vector, and $\mathbf{n}$ the unit normal vector of $\Sigma(\boldsymbol{\eta})$ defined in eq. (2). If the direction of fault slip is parallel to the projection of a relative plate motion vector $\mathbf{V}_{pl} = V_{pl}(h_1, h_2, 0)$ on the plate interface, the unit slip-direction vector $\boldsymbol{\nu}$ is given by

$$\boldsymbol{\nu} = \begin{pmatrix} \nu_1 \\ \nu_2 \\ \nu_3 \end{pmatrix} = \frac{1}{\sqrt{1 + (n_1 h_1 + n_2 h_2)^2 / n_3^2}} \begin{pmatrix} -h_1 \\ -h_2 \\ (n_1 h_1 + n_2 h_2)/n_3 \end{pmatrix}. \tag{6}$$

Thus, substituting eqs (4) and (5) into eq. (3), we obtain general expressions for the displacement field due to fault slip as

$$u_i(\mathbf{x}, t) = \int_0^t \mathrm{d}t' \int_{\Sigma} U_i(\mathbf{x}, t - t'; \boldsymbol{\eta}, 0)\, \dot{w}(\boldsymbol{\eta}, t')\, \mathrm{d}\boldsymbol{\eta} \quad t \geq 0 \tag{7}$$

with

$$U_i(\mathbf{x}, t; \boldsymbol{\eta}, t') = \mu \partial_q G_{ip}(\mathbf{x}, t; \boldsymbol{\eta}, t')[\nu_p(\boldsymbol{\eta}) n_q(\boldsymbol{\eta}) + \nu_q(\boldsymbol{\eta}) n_p(\boldsymbol{\eta})]. \tag{8}$$

Here, $U_i(\mathbf{x}, t; \boldsymbol{\eta}, t')$ denote the quasi-static displacement response functions for a unit step-slip at a point $\boldsymbol{\eta}$ on the plate interface.

Now, we divide the plate interface Σ into a seismogenic region Σ_s and the remaining steady-slip region $\Sigma - \Sigma_s$ as shown in Fig. 1. The fault-slip motion $w(\boldsymbol{\eta}, t)$ in the seismogenic region can be represented by the superposition of steady slip at the rate of relative plate motion $V_{pl}(\boldsymbol{\eta})$ and its perturbation $w_s(\boldsymbol{\eta}, t)$, and then

$$w(\boldsymbol{\eta}, t) = \begin{cases} V_{pl}(\boldsymbol{\eta})\, t + w_s(\boldsymbol{\eta}, t) & \text{on } \Sigma_s \\ V_{pl}(\boldsymbol{\eta})\, t & \text{on } \Sigma - \Sigma_s \end{cases} \quad t \geq 0. \tag{9}$$

In this study, we simply suppose that the slip perturbation is periodic in the seismogenic region:

$$w_s(\boldsymbol{\eta}, t) = -\dot{w}_s(\boldsymbol{\eta}) t + \dot{w}_s(\boldsymbol{\eta}) T \sum_{k=1}^{n} H(t - kT) \quad (n+1)T > t \geq 0, \tag{10}$$

where $H(t)$ is the Heaviside function, and T denotes the recurrence interval of interplate earthquakes.

As the time lag $t - t'$ increases, the quasi-static displacement response functions $U_i(\mathbf{x}, t; \boldsymbol{\eta}, t')$ in eq. (8) tend to certain constants, $U_i^{\infty}(\mathbf{x}; \boldsymbol{\eta}) \equiv U_i(\mathbf{x}, \infty; \boldsymbol{\eta}, 0)$, which can be easily computed by using an equivalence theorem in linear viscoelasticity (Fukahata & Matsu'ura 2006). Then, assuming the recurrence interval T to be longer than the effective relaxation time τ_e of the lithosphere–asthenosphere system, we can write eq. (7) for an interseismic calm period after the latest interplate earthquake at $t = nT$ as

$$\begin{aligned} u_i(\mathbf{x}, t) = {} & c_i(\mathbf{x}) + (t - \tau_e) \int_{\Sigma} U_i^{\infty}(\mathbf{x}; \boldsymbol{\eta}) V_{pl}(\boldsymbol{\eta})\, \mathrm{d}\boldsymbol{\eta} \\ & - (t - \tau_e) \int_{\Sigma_s} U_i^{\infty}(\mathbf{x}; \boldsymbol{\eta})\, \dot{w}_s(\boldsymbol{\eta})\, \mathrm{d}\boldsymbol{\eta} \\ & + T \int_{\Sigma_s} [U_i(\mathbf{x}, t - nT; \boldsymbol{\eta}, 0) - U_i(\mathbf{x}, 0; \boldsymbol{\eta}, 0)] \dot{w}_s(\boldsymbol{\eta})\, \mathrm{d}\boldsymbol{\eta} \\ & (n+1)T > t > nT \end{aligned} \tag{11}$$

with

$$c_i(\mathbf{x}) = \int_0^{\tau_e} \mathrm{d}t' \int_{\Sigma} U_i(\mathbf{x}, t - t'; \boldsymbol{\eta}, 0)\, \dot{w}(\boldsymbol{\eta}, t') \mathrm{d}\boldsymbol{\eta}. \tag{12}$$

The first constant term on the right side of eq. (11) represents some non-linear effect associated with the sudden initiation of steady plate subduction at $t = 0$. The second and third terms represent the surface displacements due to steady forward slip at $V_{pl}(\boldsymbol{\eta})$ over the whole plate interface and steady backward slip at $\dot{w}_s(\boldsymbol{\eta})$ in the seismogenic region, respectively. The last term represents the surface displacements due to postseismic stress relaxation in the asthenosphere.

Differentiating both sides of eq. (11) with respect to t, we obtain the expressions of interseismic surface velocities due to slip deficit at the plate interface as

$$\begin{aligned} \dot{u}_i(\mathbf{x}, t) = {} & \int_{\Sigma} U_i^{\infty}(\mathbf{x}; \boldsymbol{\eta})\, V_{pl}(\boldsymbol{\eta})\, \mathrm{d}\boldsymbol{\eta} - \int_{\Sigma_s} U_i^{\infty}(\mathbf{x}; \boldsymbol{\eta})\, \dot{w}_s(\boldsymbol{\eta})\, \mathrm{d}\boldsymbol{\eta} \\ & + T \int_{\Sigma_s} \dot{U}_i(\mathbf{x}, t - nT; \boldsymbol{\eta}, 0) \dot{w}_s(\boldsymbol{\eta})\, \mathrm{d}\boldsymbol{\eta} \quad (n+1)T > t > nT. \end{aligned} \tag{13}$$

The first and second terms on the right side of eq. (13) represent surface velocities due to steady slip over the whole plate interface and steady slip-deficit in the seismogenic region, respectively, and the third term represents the surface velocities due to postseismic stress relaxation in the asthenosphere. The viscosity of the asthenosphere has been estimated to be 4×10^{19}Pa s on global average (Cathles 1975), but it takes a somewhat smaller value (5×10^{18}Pa s) than the global average in subduction zones (Matsu'ura & Iwasaki 1983), and so the third term exponentially decays with time after the event at a time constant of tens of year. Then, except for the early stage of the earthquake cycle, we may approximate eq. (13) as

$$\dot{u}_i(\mathbf{x}) = \int_{\Sigma} U_i^{\infty}(\mathbf{x}; \boldsymbol{\eta})\, V_{pl}(\boldsymbol{\eta})\, \mathrm{d}\boldsymbol{\eta} - \int_{\Sigma_s} U_i^{\infty}(\mathbf{x}; \boldsymbol{\eta})\, \dot{w}_s(\boldsymbol{\eta})\, \mathrm{d}\boldsymbol{\eta}. \tag{14}$$

In most analyses of interseismic crustal movements, on the back-slip concept by Savage (1983), the first term (effects of steady plate subduction) has been assumed to be zero. However, as demonstrate by Matsu'ura & Sato (1989), the back-slip concept is not applicable to the case of convergent plate boundaries.

2.2 Observation equations for displacement data

The slip perturbation is not necessarily parallel to the direction of steady slip. So, in addition to the slip-deficit rate $\dot{w}_s(\boldsymbol{\eta})$ in eq. (10), which is the primary component parallel to the direction of steady slip and represented by $\dot{w}_s^{\mathrm{P}}(\boldsymbol{\eta})$ hereafter, we need to consider a complementary component $\dot{w}_s^{\mathrm{C}}(\boldsymbol{\eta})$ perpendicular to the direction of steady slip. Then, we represent the distribution of each slip-deficit rate component on $\Sigma_s(\boldsymbol{\eta})$ by the superposition of a finite number of known basis functions $\Phi_l(\eta_1,\eta_2)$ $(l = 1, ..., L)$ defined on a $\eta_1-\eta_2$ plane parallel to the Earth's surface ($x_3 = 0$):

$$\dot{w}_s^{\mathrm{P}}(\boldsymbol{\eta})\mathrm{d}\Sigma(\boldsymbol{\eta}) = \frac{1}{n_3(\boldsymbol{\eta})}\sum_{l=1}^{L} a_l^{\mathrm{P}}\Phi_l(\eta_1,\eta_2)\,\mathrm{d}\eta_1\mathrm{d}\eta_2, \tag{15}$$

$$\dot{w}_s^{\mathrm{C}}(\boldsymbol{\eta})\mathrm{d}\Sigma(\boldsymbol{\eta}) = \frac{1}{n_3(\boldsymbol{\eta})}\sum_{l=1}^{L} a_l^{\mathrm{C}}\Phi_l(\eta_1,\eta_2)\,\mathrm{d}\eta_1\mathrm{d}\eta_2. \tag{16}$$

Using the above expressions, we can rewrite eq. (14), for example, as

$$\dot{u}_i(\mathbf{x}) = \dot{u}_i^{\mathrm{ss}}(\mathbf{x}) + \sum_{l=1}^{L} a_l^{\mathrm{P}}U_{il}^{\mathrm{P}}(\mathbf{x}) + \sum_{l=1}^{L} a_l^{\mathrm{C}}U_{il}^{\mathrm{C}}(\mathbf{x}) \tag{17}$$

with

$$\dot{u}_i^{\mathrm{ss}}(\mathbf{x}) = \int_{\Sigma} U_i^{\infty}(\mathbf{x};\boldsymbol{\eta})\,V_{\mathrm{pl}}(\boldsymbol{\eta})\,\mathrm{d}\boldsymbol{\eta} \tag{18}$$

and

$$U_{il}^{\mathrm{P}}(\mathbf{x}) = -\int\int \frac{1}{n_3(\boldsymbol{\eta})}U_i^{\infty}(\mathbf{x};\boldsymbol{\eta})\Phi_l(\eta_1,\eta_2)\,\mathrm{d}\eta_1\mathrm{d}\eta_2, \tag{19}$$

$$U_{il}^{\mathrm{C}}(\mathbf{x}) = -\int\int \frac{1}{n_3(\boldsymbol{\eta})}U_i^{\prime\infty}(\mathbf{x};\boldsymbol{\eta})\Phi_l(\eta_1,\eta_2)\,\mathrm{d}\eta_1\mathrm{d}\eta_2. \tag{20}$$

Here, $\dot{u}_i^{\mathrm{ss}}(\mathbf{x})$ in eq. (18) are the surface velocities due to steady plate subduction, computed for a given global plate motion model, and $U_i'^{\infty}(\mathbf{x};\boldsymbol{\eta})$ in eq. (20) denote the quasi-static displacement response functions at $t = \infty$ for the complementary slip component, defined by

$$U_i'^{\infty}(\mathbf{x};\boldsymbol{\eta}) = \mu\partial_q G_{ip}(\mathbf{x},\infty;\boldsymbol{\eta},0)\left[\nu_p'(\boldsymbol{\eta})n_q(\boldsymbol{\eta}) + \nu_q'(\boldsymbol{\eta})n_p(\boldsymbol{\eta})\right]. \tag{21}$$

In the above equation, $\boldsymbol{\nu}'(\boldsymbol{\eta})$ represents the unit vector on $\Sigma_s(\boldsymbol{\eta})$ perpendicular to the direction of steady slip.

Thus, for given surface velocity data $\dot{u}_i^{\mathrm{obs}}$ $(i = 1, 2)$ at points $\mathbf{x} = \mathbf{x}_k$ $(k = 1, ..., K)$, we obtain an observation equation in vector form:

$$\dot{\mathbf{u}}^{\mathrm{obs}} = \dot{\mathbf{u}}^{\mathrm{ss}} + \mathbf{U}\mathbf{a} + \mathbf{e}^{\mathrm{obs}}. \tag{22}$$

Here, $\dot{\mathbf{u}}^{\mathrm{obs}}$ and $\dot{\mathbf{u}}^{\mathrm{ss}}$ are $2K \times 1$ dimensional data vectors with the elements $\dot{u}_i^{\mathrm{obs}}(\mathbf{x}_k)$ and $\dot{u}_i^{\mathrm{ss}}(\mathbf{x}_k)$, respectively, $\mathbf{e}^{\mathrm{obs}}$ is a $2K \times 1$ dimensional error vectors, $\mathbf{a}$ is a $2L \times 1$ dimensional model parameter vector composed of $\mathbf{a}^{\mathrm{P}}$ with the elements a_l^{P} $(l = 1, ..., L)$ and $\mathbf{a}^{\mathrm{C}}$ with the elements a_l^{C} $(l = 1, ..., L)$, and $\mathbf{U}$ is a $2K \times 2L$ dimensional coefficient matrix composed of $\mathbf{U}^{\mathrm{P}}$ and $\mathbf{U}^{\mathrm{C}}$, whose elements are numerically calculated from eqs (19) and (20), respectively. Subtracting the theoretically computed velocities $\dot{\mathbf{u}}^{\mathrm{ss}}$ from the both sides of eq. (22), we obtain the following observation equation for the residual velocities $\dot{\mathbf{u}}^{\mathrm{res}} \equiv \dot{\mathbf{u}}^{\mathrm{obs}} - \dot{\mathbf{u}}^{\mathrm{ss}}$:

$$\dot{\mathbf{u}}^{\mathrm{res}} = \mathbf{U}\mathbf{a} + \mathbf{e}^{\mathrm{res}}. \tag{23}$$

We solve the above observation equation for the model parameters $\mathbf{a}$. Given the optimum solution, we can calculate the optimum slip-deficit rate distributions, $\dot{w}_s^{\mathrm{P}}(\boldsymbol{\eta})$ and $\dot{w}_s^{\mathrm{C}}(\boldsymbol{\eta})$, from eqs (15) and (16), respectively.

2.3 Transformation of GPS velocity data into strain rates

The displacement data obtained by GPS measurements, which are the difference between the current and previous coordinates of observation stations, contain systematic errors due to the rigid translation and rotation of crustal blocks, which cannot be explained by the present theoretical model in eq. (13) or (14). As shown in Appendix, one of the effective ways to remove the rigid block translation and rotation from GPS array data is to transform observed horizontal displacement vectors into average strain tensors for individual triangles composed of adjacent GPS stations.

Applying the transformation rule in eq. (A19) to every element of a GPS triangular mesh, we can define a transformation matrix $\mathbf{R}$ for a whole data set, composed of the sub-matrices $\mathbf{R}_{klm} = \mathbf{A}_{klm}\mathbf{B}_{klm}$ for triangle elements $\Delta P_k P_l P_m$. Then, premultiplying both sides of eq. (23) by the transformation matrix $\mathbf{R}$, we obtain an observation equation for GPS strain rates:

$$\mathbf{d} = \mathbf{H}\mathbf{a} + \mathbf{e} \tag{24}$$

with

$$\mathbf{d} = \mathbf{R}\dot{\mathbf{u}}^{\mathrm{res}},\ \mathbf{H} = \mathbf{R}\mathbf{U},\ \mathbf{e} = \mathbf{R}\mathbf{e}^{\mathrm{res}}. \tag{25}$$

Here, $\mathbf{d}$ is a $N \times 1$ dimensional ($N = 3\times$number of triangle elements) data vector, $\mathbf{a}$ is a $M \times 1$ dimensional ($M = 2L$) model parameter vector, $\mathbf{H}$ is a $N \times M$ dimensional coefficient matrix, and $\mathbf{e}$ is a $N \times 1$ dimensional error vector. Note that the number of triangle elements, and so the number of strain rate data, depends on how we construct the triangular mesh from GPS stations. In addition, to complete the description of the observation equation in eq. (24), we must specify the statistical properties of data errors $\mathbf{e}$.

The data errors $\mathbf{e}^{\mathrm{res}}$ in eq. (23) generally consist of observation errors $\mathbf{e}^{\mathrm{obs}}$ in GPS measurements and modelling errors $\mathbf{e}^{\mathrm{mod}}$ due to imperfection in theoretical models:

$$\mathbf{e}^{\mathrm{res}} = \mathbf{e}^{\mathrm{obs}} + \mathbf{e}^{\mathrm{mod}}. \tag{26}$$

Then the data errors $\mathbf{e}$ in eq. (24) can be written as

$$\mathbf{e} \equiv \mathbf{R}\mathbf{e}^{\mathrm{res}} = \mathbf{R}\mathbf{e}^{\mathrm{obs}} + \mathbf{R}\mathbf{e}^{\mathrm{mod}}. \tag{27}$$

Here, we simply assume the transformed observation errors $\mathbf{R}\mathbf{e}^{\mathrm{obs}}$ and modelling errors $\mathbf{R}\mathbf{e}^{\mathrm{mod}}$ to be uncorrelated and their statistical properties to be Gaussian with zero mean and covariance matrices $\sigma_{\mathrm{obs}}^2\mathbf{E}_{\mathrm{obs}}$ and $\sigma_{\mathrm{mod}}^2\mathbf{E}_{\mathrm{mod}}$, respectively. Then, the data errors $\mathbf{e}$ also obey Gaussian distribution,

$$\mathbf{e} \sim N(\mathbf{0}, \sigma^2\mathbf{E}), \tag{28}$$

with zero mean and the covariance matrix

$$\sigma^2\mathbf{E} = \sigma_{\mathrm{obs}}^2\mathbf{E}_{\mathrm{obs}} + \sigma_{\mathrm{mod}}^2\mathbf{E}_{\mathrm{mod}}. \tag{29}$$

In the case of GPS velocity data, correlation between observation errors $\mathbf{e}^{\mathrm{obs}}$ is weak and their variances are almost the same, and so we may write $\mathbf{E}_{\mathrm{obs}}$ in eq. (29) as $\mathbf{R}\mathbf{R}^{\mathrm{T}}$ following the error propagation rule. On the other hand, the modelling errors $\mathbf{e}^{\mathrm{mod}}$ such as rigid block translation and rotation have significant long-range correlation. However, transforming $\mathbf{e}^{\mathrm{mod}}$ into $\mathbf{R}\mathbf{e}^{\mathrm{mod}}$, we can resolve the long-range correlation between modelling errors. So, assuming weak correlation between unresolved modelling errors, we may regard $\mathbf{E}_{\mathrm{mod}}$ in eq. (29) as a diagonal matrix $\mathbf{D}$. From such

consideration, we set the basic structure of the covariance matrix of data errors **e** as

$$\sigma^2\mathbf{E} = \sigma^2(\mathbf{R}\mathbf{R}^{\mathrm{T}} + c^2\mathbf{D}). \tag{30}$$

Here, we treated σ^2_{obs} as an unknown scale factor σ^2, because we know only its rough estimate. The parameter c^2 ($= \sigma^2_{\mathrm{mod}}/\sigma^2$) was introduced to control the relative weight of modelling errors to observation errors. Note that taking $c^2 \to 0$ means regarding theoretically unexplainable coherent noise as signal.

The matrix $\mathbf{A}_{klm}$ in eq. (A19) has a premultiplying factor, the inverse of which is given by the product of the side-lengths l_{ij} ($ij = kl, lm, mk$) and the sine of internal angles s_i ($i = k, l, m$) of a triangle element. Then, from the first term on the right side of eq. (30), we can see that the observation errors $\mathbf{e}^{\mathrm{obs}}$ are enormously amplified by the displacement-strain transformation, if any side-length or internal angle of the triangle element takes a very small value. To avoid this problem, as pointed out by Feigl *et al.* (1990), we have to construct the triangular mesh so that the shape of every element becomes as close to the equilateral triangle as possible. The optimum triangular mesh in such a sense can be constructed by using the method of Delaunay triangulation (e.g. De Berg *et al.* 1997).

2.4 Bayesian model and inversion formula

Finally, following Matsu'ura *et al.* (2007), we construct a Bayesian model by incorporating direct and indirect prior information into observed data. From eq. (24), on the assumption of Gaussian distribution of data errors in eq. (28), we obtain a stochastic model that relates the observed data **d** with the model parameters **a** as

$$p(\mathbf{d}|\,\mathbf{a};\sigma^2) = (2\pi\sigma^2)^{-N/2}\,|\mathbf{E}|^{-1/2} \times \exp\left[-\frac{1}{2\sigma^2}(\mathbf{d}-\mathbf{H}\mathbf{a})^{\mathrm{T}}\mathbf{E}^{-1}(\mathbf{d}-\mathbf{H}\mathbf{a})\right], \tag{31}$$

where σ^2 is an unknown scale factor, and $|\mathbf{E}|$ denotes the determinant of **E** in eq. (30).

In addition to the observed data, we have two different sorts of prior information; that is, direct prior information about the most plausible values of slip-deficit rates and indirect prior information about the degree of spatial variation in slip-deficit rates. From plate tectonics, we may postulate that slip-deficit rate vectors are almost parallel to the direction of plate convergence, and their most plausible values are zero. Then the direct prior information about the model parameters, $\mathbf{a}^{\mathrm{P}}$ and $\mathbf{a}^{\mathrm{C}}$, can be written in the form of probability density function (pdf) as

$$r_1(\mathbf{a};\varepsilon^2) = (2\pi\varepsilon^2)^{-M/2}\,|\mathbf{F}|^{-1/2}\exp\left[-\frac{1}{2\varepsilon^2}\mathbf{a}^{\mathrm{T}}\mathbf{F}^{-1}\mathbf{a}\right], \tag{32}$$

where ε^2 is an unknown scale factor, and **F** denotes a $M \times M$ positive definite matrix given by

$$\mathbf{F} = \begin{bmatrix} \gamma^2\mathbf{I}_{\mathrm{P}} & \mathbf{O} \\ \mathbf{O} & \mathbf{I}_{\mathrm{C}} \end{bmatrix}. \tag{33}$$

Here, following Matsu'ura *et al.* (2007), we introduced the parameter γ^2 (>1) to quantitatively represent the postulate that slip-deficit rate vectors are almost parallel to the direction of plate convergence. If the postulate is very strict, we should take the value of γ^2 to be infinity (no direct constraint for $\mathbf{a}^{\mathrm{P}}$). If the postulate is very loose, we should take the value of γ^2 to be unity.

On the other hand, from physical consideration, we may postulate that the spatial distribution of slip-deficit rates must be smooth in some degree. Following Yabuki & Matsu'ura (1992), we define the roughness g written in the positive-definite quadratic form of the model parameters, $\mathbf{a}^{\mathrm{P}}$ and $\mathbf{a}^{\mathrm{C}}$, as

$$g = (\mathbf{a}^{\mathrm{P}})^{\mathrm{T}}\mathbf{G}^{\mathrm{P}}\mathbf{a}^{\mathrm{P}} + (\mathbf{a}^{\mathrm{C}})^{\mathrm{T}}\mathbf{G}^{\mathrm{C}}\mathbf{a}^{\mathrm{C}} = \mathbf{a}^{\mathrm{T}}\mathbf{G}\mathbf{a}, \tag{34}$$

where $\mathbf{G}^{\mathrm{P(C)}}$ are $L \times L$ symmetric matrices, the ij elements of which are given by

$$G_{ij}^{\mathrm{P(C)}} = \sum_{k=1}^{2}\sum_{l=1}^{2} \times \iint \frac{1}{n_3(\boldsymbol{\eta})}\frac{1}{s_k^2(\boldsymbol{\eta})s_l^2(\boldsymbol{\eta})}\frac{\partial^2\Phi_i(\eta_1,\eta_2)}{\partial\eta_k\partial\eta_l}\frac{\partial^2\Phi_j(\eta_1,\eta_2)}{\partial\eta_k\partial\eta_l}\mathrm{d}\eta_1\mathrm{d}\eta_2 \tag{35}$$

with

$$s_i(\boldsymbol{\xi}) = \sqrt{1 + n_i^2(\boldsymbol{\xi})/n_3^2(\boldsymbol{\xi})}. \tag{36}$$

Then the indirect prior information can be written in the form of pdf as

$$r_2(\mathbf{a};\rho^2) = (2\pi\rho^2)^{-M/2}\,|\mathbf{G}|^{1/2}\exp\left[-\frac{1}{2\rho^2}\mathbf{a}^{\mathrm{T}}\mathbf{G}\mathbf{a}\right]. \tag{37}$$

Combining $r_1(\mathbf{a};\varepsilon^2)$ and $r_2(\mathbf{a};\rho^2)$ in a proper way (Fukahata *et al.* 2004), we obtain the pdf form of total prior information about the model parameters **a**:

$$q(\mathbf{a};\rho^2;\varepsilon^2) = (2\pi)^{-M/2}\left|\rho^{-2}\mathbf{G} + \varepsilon^{-2}\mathbf{F}^{-1}\right|^{1/2} \times \exp\left[-\frac{1}{2}\mathbf{a}^{\mathrm{T}}(\rho^{-2}\mathbf{G} + \varepsilon^{-2}\mathbf{F}^{-1})\mathbf{a}\right]. \tag{38}$$

We now construct a Bayesian model by combining $q(\mathbf{a};\rho^2;\varepsilon^2)$ in eq. (38) and $p(\mathbf{d}|\,\mathbf{a};\sigma^2)$ in eq. (31) by Bayes' rule:

$$p(\mathbf{a};\sigma^2,\alpha^2,\beta^2|\,\mathbf{d}) = c(2\pi\sigma^2)^{-(M+N)/2}\,|\mathbf{E}|^{-1/2}\left|\alpha^2\mathbf{G} + \beta^2\mathbf{F}^{-1}\right|^{1/2} \times \exp\left[-\frac{1}{2\sigma^2}s(\mathbf{a})\right] \tag{39}$$

with

$$s(\mathbf{a}) = (\mathbf{d}-\mathbf{H}\mathbf{a})^{\mathrm{T}}\mathbf{E}^{-1}(\mathbf{d}-\mathbf{H}\mathbf{a}) + \mathbf{a}^{\mathrm{T}}\left(\alpha^2\mathbf{G} + \beta^2\mathbf{F}^{-1}\right)\mathbf{a}. \tag{40}$$

Here, $\alpha^2 \equiv \sigma^2/\rho^2$ and $\beta^2 \equiv \sigma^2/\varepsilon^2$ are hyperparameters that control the relative weights of the indirect and direct prior information to the observed data, respectively. To determine the optimum values of the hyperparameters, we can use a Bayesian information criterion (ABIC) proposed by Akaike (1980), the explicit expression of which is given in Matsu'ura *et al.* (2007) as

$$\begin{aligned}\mathrm{ABIC}(\alpha^2,\beta^2|\mathbf{d}) &\equiv -2\log\int_{-\infty}^{+\infty} p(\mathbf{a};\sigma^2,\alpha^2,\beta^2|\,\mathbf{d})\mathrm{d}\mathbf{a} + C \\ &= N\log s(\mathbf{a}^*) - \log\left|\alpha^2\mathbf{G} + \beta^2\mathbf{F}^{-1}\right| \\ &\quad + \log\left|\mathbf{H}^{\mathrm{T}}\mathbf{E}^{-1}\mathbf{H} + \alpha^2\mathbf{G} + \beta^2\mathbf{F}^{-1}\right| + C'\end{aligned} \tag{41}$$

with

$$\mathbf{a}^* = (\mathbf{H}^{\mathrm{T}}\mathbf{E}^{-1}\mathbf{H} + \alpha^2\mathbf{G} + \beta^2\mathbf{F}^{-1})^{-1}\mathbf{H}^{\mathrm{T}}\mathbf{E}^{-1}\mathbf{d}, \tag{42}$$

where $\mathbf{a}^*$ denotes the $M \times 1$ dimensional solution vector that maximizes the posterior pdf in eq. (39) for certain fixed values of α^2 and β^2, and C' is a term independent of α^2 and β^2. The optimum values of α^2 and β^2 that minimize ABIC can be found by iterative numerical search. Once the optimum values of α^2 and β^2 are found, denoting them by $\hat{\alpha}^2$ and $\hat{\beta}^2$, we can obtain the optimum model parameters $\hat{\mathbf{a}}$ and the covariance matrix $\mathbf{C}(\hat{\mathbf{a}})$ of their estimation errors as

$$\hat{\mathbf{a}} = (\mathbf{H}^{\mathrm{T}}\mathbf{E}^{-1}\mathbf{H} + \hat{\alpha}^2\mathbf{G} + \hat{\beta}^2\mathbf{F}^{-1})^{-1}\mathbf{H}^{\mathrm{T}}\mathbf{E}^{-1}\mathbf{d}, \tag{43}$$

$$\mathbf{C}(\hat{\mathbf{a}}) = \hat{\sigma}^2(\mathbf{H}^{\mathrm{T}}\mathbf{E}^{-1}\mathbf{H} + \hat{\alpha}^2\mathbf{G} + \hat{\beta}^2\mathbf{F}^{-1})^{-1} \tag{44}$$

with

$$\hat{\sigma}^2 = s(\hat{\mathbf{a}})/N. \tag{45}$$

3 APPLICATION TO GPS DATA IN THE KANTO REGION

We demonstrate the applicability of the inversion method developed in the previous section through the analysis of interseismic GPS array data in the Kanto region, central Japan. In this region the Pacific (PAC) plate is descending beneath the North American (NAM) and Philippine Sea (PHS) plates, and the PHS plate is descending beneath the NAM plate and running on the PAC plate at its eastern margin (Ishida 1992; Hashimoto *et al.* 2004) as shown in Fig. 2. The eastern part of the NAM-PHS plate interface is a seismogenic region, where the Genroku–Kanto (M8.1) and Taisho–Kanto (M7.9) earthquakes have occurred in 1703 and 1923, respectively. The western part is also a seismogenic region, which has ruptured at the time of the 1854 Ansei–Tokai earthquake (M8.4). On the other hand, the northern part is a locked region, where the Izu peninsula is colliding with the Mainland of Japan. For computation of the displacement response functions in eq. (13) or (14), we used an elastic-viscoelastic layered half-space model under gravity, where the rigidity and thickness of the elastic surface layer were taken to be 40 GPa and 60 km, respectively, and the viscosity of the underlying viscoelastic half-space to be 5×10^{18} Pa s on the analysis of coseismic and postseismic crustal movements associated with the 1923 Kanto earthquake by Matsu'ura & Iwasaki (1983).

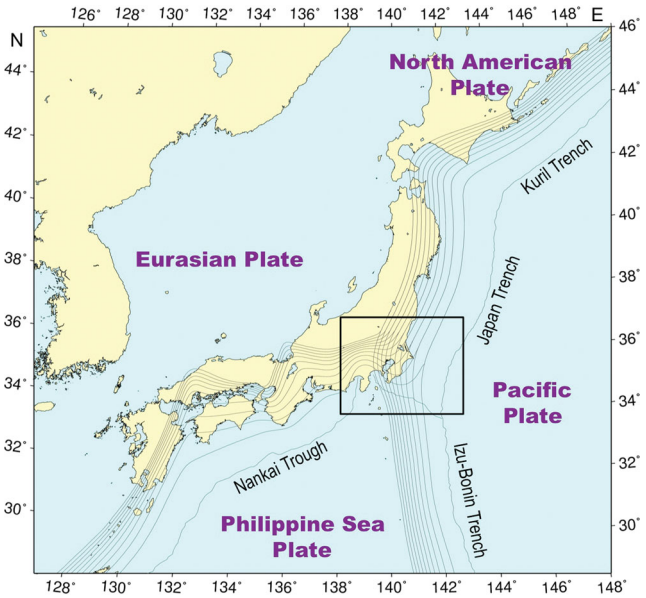

Figure 2. Tectonic setting and 3-D geometry of plate interfaces in the Japan region. The upper surfaces of the Pacific and Philippine Sea plates, descending beneath the North American/Philippine Sea plates and the North American/Eurasian plates, respectively, are represented by the grey iso-depth contours at intervals of 10 km. The central rectangle shows the model region for inversion analysis.

3.1 Data and model setting

To monitor the crustal movements of the Japanese Islands, a nationwide dense GPS network (GEONET) has been operated by Geographical Survey Institute of Japan (now Geospatial Information Authority of Japan) since 1996. Applying a least-squares collocation method to GPS daily coordinate data for the interseismic calm period of 1996–2000, Sagiya (2004) has obtained a set of horizontal velocities at GEONET stations in the Kanto region. In the present analysis, we use basically the same dataset as this one after removing the data of the following GPS stations: (1) all stations at volcanic islands along the Izu–Bonin arc, (2) three stations near Ito, the northeastern part of the Izu peninsula, strongly affected by the 1998 earthquake swarm off Ito (Nishimura 2002) and (3) five stations near the indefinite plate boundary in the Izu–Mainland collision zone. In Fig. 3(a), we show the GPS horizontal velocities used in the present analysis. According to Sagiya (2004), the standard deviations (observation errors) of these velocity data are in the range of 1–3 mm yr^{-1}. It should be noted that these data contain not only interseismic deformation due to slip deficit at plate interfaces but also long-term deformation due to steady plate subduction.

From ISC (International Seismological Centre) hypocentre data, Hashimoto *et al.* (2004) have constructed a realistic 3-D model of plate interface geometry in and around Japan as shown in Fig. 2. In this model, the depth ($z = -x_3$) to each plate interface is represented as a continuous and differentiable (up to the second order) function, $z = -f(x_1, x_2)$, by superposing bi-cubic B-splines with equally spaced local supports in the x_1- and x_2-directions. So, from eq. (2), we can compute the unit normal vector $\mathbf{n}(\boldsymbol{\eta})$ of the plate interfaces $\Sigma(\boldsymbol{\eta})$ everywhere. The 3-D geometry of plate interfaces has been modelled by also Nakajima & Hasegawa (2006) for northeast Japan, Hirose *et al.* (2008) for central Japan, and Nakajima & Hasegawa (2007) for southwest Japan. In their models, however, the depths to plate interfaces are given only at grid points, and so the continuity and differentiability of plate interfaces are not guaranteed everywhere. In our model, given global plate motion (NUVEL-1A; DeMets *et al.* 1994), we can compute the magnitude $V_{\mathrm{pl}}(\boldsymbol{\eta})$ and direction $\boldsymbol{v}(\boldsymbol{\eta})$ of steady slip vectors from eq. (6) at any point on the plate interfaces. Then the long-term surface velocities due to steady plate subduction at GPS stations are obtained by evaluating the first term on the right side of eq. (13) and also eq. (14) as shown in Fig. 3(b). Subtracting the computed long-term surface velocities from the observed GPS velocities, we obtain the residuals $\dot{\mathbf{u}}^{\mathrm{res}}$ in eq. (23) as shown in Fig. 3(c).

In the Kanto region, the descending PHS plate directly contacts with the NAM and PAC plates on its upper and lower sides, respectively, as shown in Fig. 4. So, as the model regions $\Sigma_{\mathrm{s}}(\boldsymbol{\eta})$, we took the blue stippled portion of the NAM-PHS plate interface and the pink-coloured portion of the PHS-PAC plate interface but not the NAM-PAC plate interface, because plate interfaces about the eastern margin of the descending PHS plate, which was once a fluid-rich subduction zone forearc, would be still weak. The spatial distribution for each of the primary and complementary components of slip-deficit rate vectors is represented by the superposition of 696 normalized bi-cubic B-splines for the NAM-PHS plate interface and 433 normalized bi-cubic B-splines for the PHS-PAC plate interface. In either case, the local supports of the bi-cubic B-splines are taken to be 8 km in both the x_1- and x_2-directions. Since the Taisho–Kanto earthquake (M7.9) occurred in 1923, this region has been in a long calm period, and so the third term (effects of post-seismic stress relaxation) in eq. (13) is negligible. Then we may use eq. (14) to analyse the GPS array data in the period of 1996–2000.

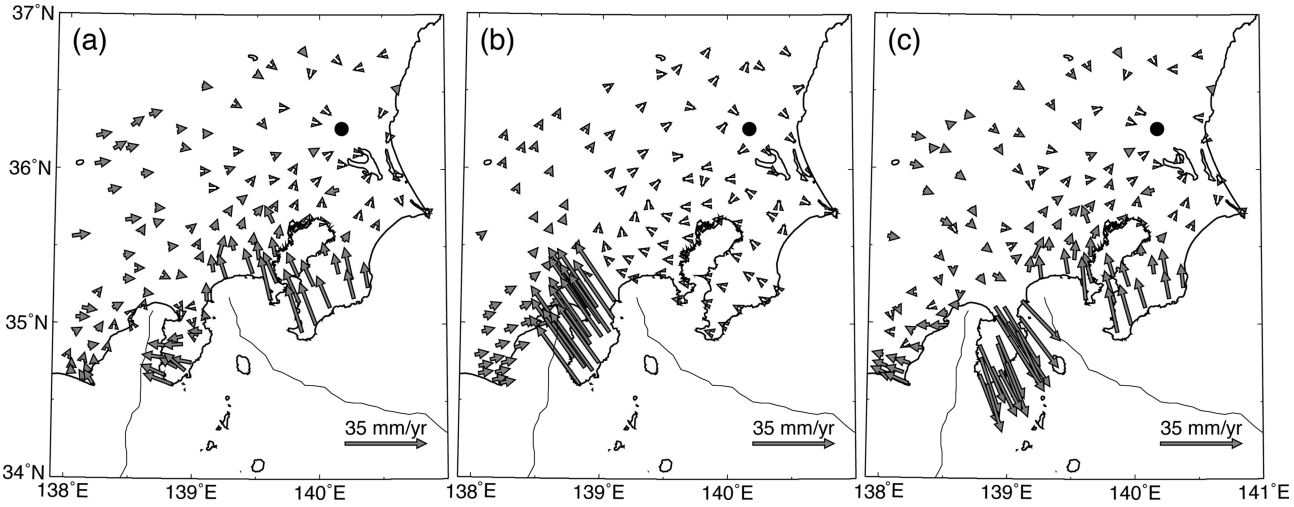

Figure 3. Interseismic horizontal velocities at GPS stations in the Kanto region, central Japan. (a) Horizontal velocities obtained from GPS measurements for 1996–2000 (Sagiya 2004). (b) Theoretical horizontal velocities due to steady plate subduction. (c) Residual horizontal velocities obtained by subtracting the theoretical velocities in (b) from the observed velocities in (a). The grey arrows represent the relative velocity vectors to a reference point YST, which is indicated by a solid circle in each diagram.

We constructed the optimum triangular mesh from the GPS stations in Fig. 3 with the method of Delaunay triangulation. Then, following eq. (25), we transformed the residual velocity vectors $\dot{\mathbf{u}}^{\mathrm{res}}$ into the average strain rates $\mathbf{d}$ and the coefficient matrix $\mathbf{U}$ into the corresponding coefficient matrix $\mathbf{H}$. In Figs 5(a) and (b), we show the transformed average strain rates in the form of dilatation and maximum shear strain, respectively, together with the optimum triangular mesh indicated by the grey solid lines. For the covariance matrix $\sigma^2\mathbf{E}$ of data errors in eq. (30), considering the systematic increase in spacing of GPS stations with distance from the NAM-PHS plate boundary, we set its explicit form as

$$E_{ij} = [\mathbf{R}\mathbf{R}^{\mathrm{T}}]_{ij} + c^2(l_i/\bar{l})^2\delta_{ij}, \tag{46}$$

where $l_i/\bar{l}$ denotes the normalized perimeter of the ith triangle. In the present case, the average spacing of GPS stations is about 20 km, and so we took the standard value of perimeter $\bar{l}$ to be 60 ($= 3 \times 20$) km. As to c^2, since modelling errors will be larger than observation errors (1–3 mm yr^{-1}), we should search its appropriate value within the range of $1 < c^2 < \infty$. In this range, the optimum estimate of σ^2 in eq. (45) decreases monotonously as c^2 increases, but it contradicts the original meaning of σ^2 in eq. (30). Such contradiction will be resolved if we could select the appropriate value of c^2 so that the optimum estimate of σ^2 accords with the variance of observation errors σ^2_{obs}. Then, we may use the accordance of the optimum estimate of σ^2 with σ^2_{obs} as a criterion to select the appropriate value of c^2, though we know only the rough estimate of σ^2_{obs}. For the direct prior information in eq. (33), on account of the rotation of the Izu microplate proposed by Nishimura *et al.* (2007) on the geodetic data inversion with a block-fault model, we took the value of γ^2 to be 9 to allow the deflection of slip-deficit rate vectors from the direction of plate convergence in the range of ± 20 degrees. In addition, we set the relative weight of smoothness parameter $(1/\rho^2)$ in eq. (37) for the PHS-PAC plate interface to the NAM-PHS plate interface to be 9 to improve the low sensitivity of model parameters on the PHS-PAC plate interface. Note that strengthening smoothness suppresses estimation errors at the expense of resolution.

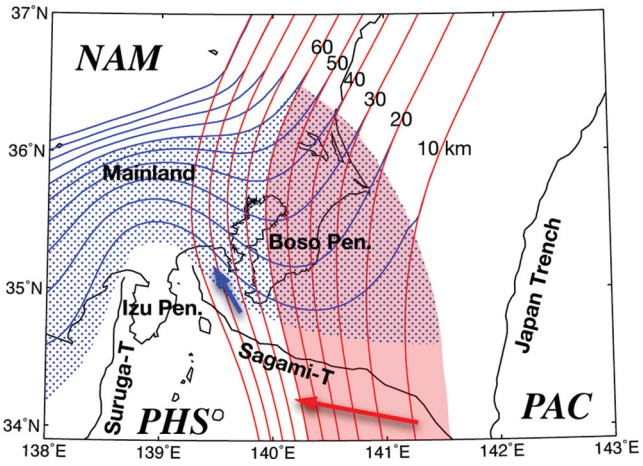

Figure 4. Plate interface geometry in the Kanto region and model setting. The blue and red iso-depth contours (10-km intervals) represent the NAM-PHS and NAM/PHS-PAC plate interfaces, respectively. The blue-stippled portion of the NAM-PHS plate interface and the pink-coloured portion of the PHS-PAC plate interface show the model regions for inversion analysis. The blue and red arrows indicate the steady slip vectors at the NAM-PHS and PHS-PAC plate interfaces, respectively. NAM, North American plate; PHS, Philippine Sea plate; PAC, Pacific plate.

3.2 Inverted slip-deficit rate distribution

Applying the inversion formula given in Section 2.4 to the strain rates transformed from the GPS velocity data, we obtained the optimum slip-deficit rate distribution on the NAM-PHS and PHS-PAC plate interfaces. We plotted ABIC for $c^2 = 10$ (most appropriate among 1, 10, 100 and 1000) as a function of the hyperparameters α^2 and β^2 in Fig. 6, where the cross indicates the minimum point that gives the optimum values of hyperparameters $\hat{\alpha}^2$ and $\hat{\beta}^2$. For these values, the optimum model parameters $\hat{\mathbf{a}}$ and the covariance matrix $\mathbf{C}(\hat{\mathbf{a}})$ of their estimation errors can be computed from eqs (43) and (44), respectively, and the optimum slip-deficit rate distribution from eqs (15) and (16).

We show the inverted slip-deficit rate distribution on the NAM-PHS and PHS-PAC plate interfaces in Figs 7(a) and (b), respectively, together with their estimation errors in Figs 8(a) and (b).

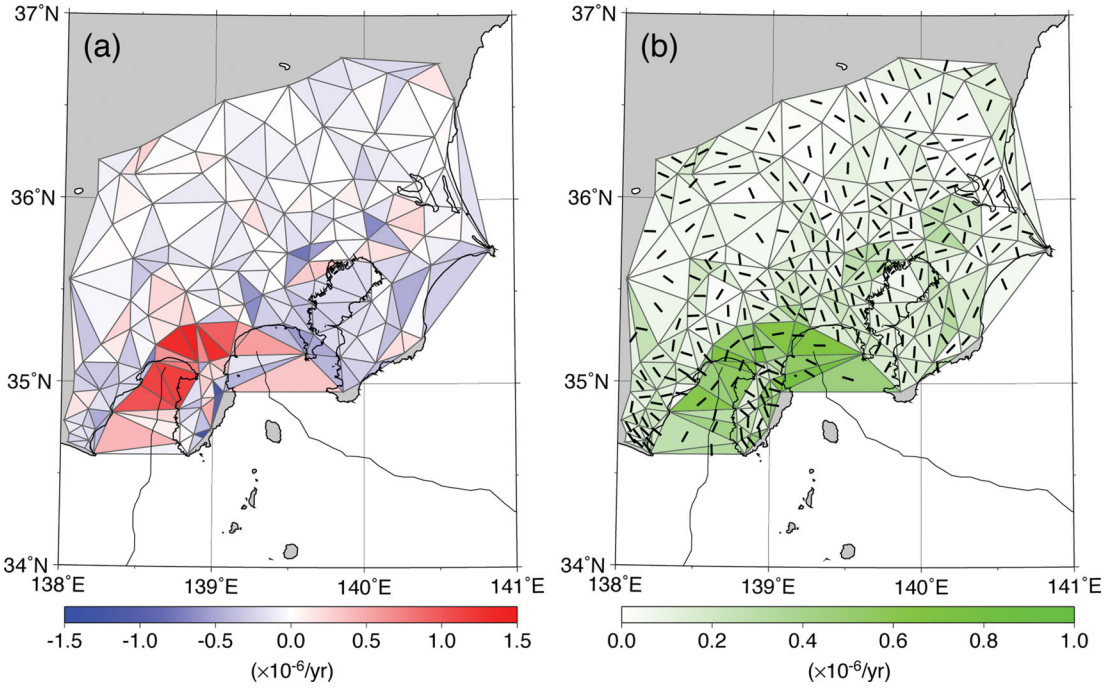

Figure 5. The horizontal strain rates transformed from GPS velocity data. (a) Dilatation. (b) Maximum shear strain. The black bar in each triangle indicates the direction of maximum horizontal contraction. The grey solid lines show the optimum triangular mesh constructed from GPS stations with Delaunay triangulation.

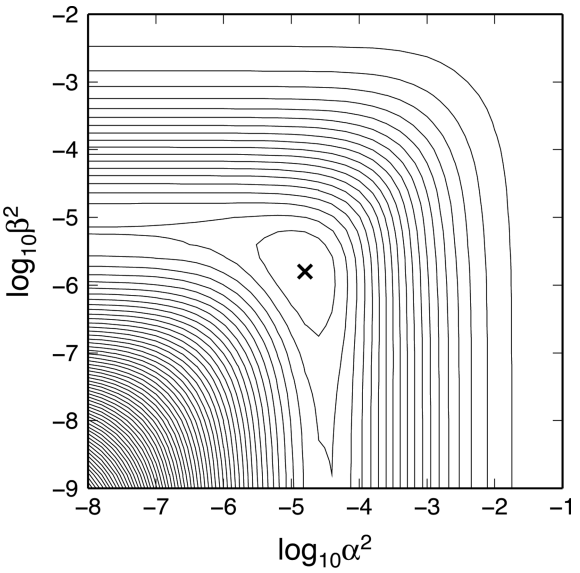

Figure 6. The contour map of ABIC plotted as a function of hyperparameters α^2 and β^2. The contour intervals are taken to be 10.0. The cross indicates the minimum point that gives the optimum values of hyperparameters.

From Fig. 7(a), we can see that the broad and high slip-deficit rate ($>20\,\mathrm{mm\,yr^{-1}}$) zone extends from southeast off the Boso peninsula to the Tokai region along the plate boundary segmented into the Sagami trough, the Izu–Mainland collision zone, and the Suruga trough. The depth range of the high slip-deficit rate zone is about 5–20 km except the collision zone, where the interplate coupling reaches 50 km in depth. In this high slip-deficit rate zone, the accumulation of tectonic stress due to plate convergence gradually proceeds during the interseismic period. The remaining part of the NAM-PHS plate interface is in the state of steady slip at plate convergence rates, and so tectonic stress does not accumulate there.

With the same plate interface geometry and inversion formula as in the present analysis, Matsu'ura *et al.* (2007) have analysed the levelling and triangulation data associated with the 1923 Kanto earthquake (M7.9), which is the last great earthquake occurred in the Sagami trough segment of the NAM-PHS plate interface. Their inversion results show that the coseismic slip of the Kanto earthquake extends from the northern end of the Sagami trough to the southern tip of the Boso peninsula in the depth range of 5–25 km with a bimodal distribution of the 5 km-deep northwestern and 15 km-deep southeastern peaks of about 8 m. The slip vectors are almost parallel to the direction of plate convergence. The good agreement between the coseismic slip pattern and the slip-deficit rate pattern obtained in the present analysis suggests that most of tectonically accumulated stress in the Sagami trough segment would be eventually released by the occurrence of a forthcoming Kanto earthquake. From the historical documents of tsunami in the Tokai district, Hatori (1976, 1977) have pointed out that the dynamic rupture of the 1854 Ansei–Tokai earthquake (M8.4) reached the Suruga trough segment. So, in this segment, the tectonic stress accumulated since 1854 would be eventually released by the occurrence of a forthcoming Tokai earthquake (e.g. Ishibashi 1981). In the Izu–Mainland collision zone, on the other hand, the accumulated tectonic stress would not be released by coseismic fault slip along the plate interface, but released by intraplate inelastic deformation such as seismic and/or aseismic slip on the active faults developed around the collision zone (Matsuda 1977; Terakawa & Matsu'ura 2010). From the estimation error distribution in Fig. 8(a), we can say that the high slip-deficit rate zones in the Sagami and Suruga trough segments are reliable, but the 30 km-deep slip-deficit rate peak in the Izu–Mainland collision zone might be attributed to the imperfection of the slip-deficit model used

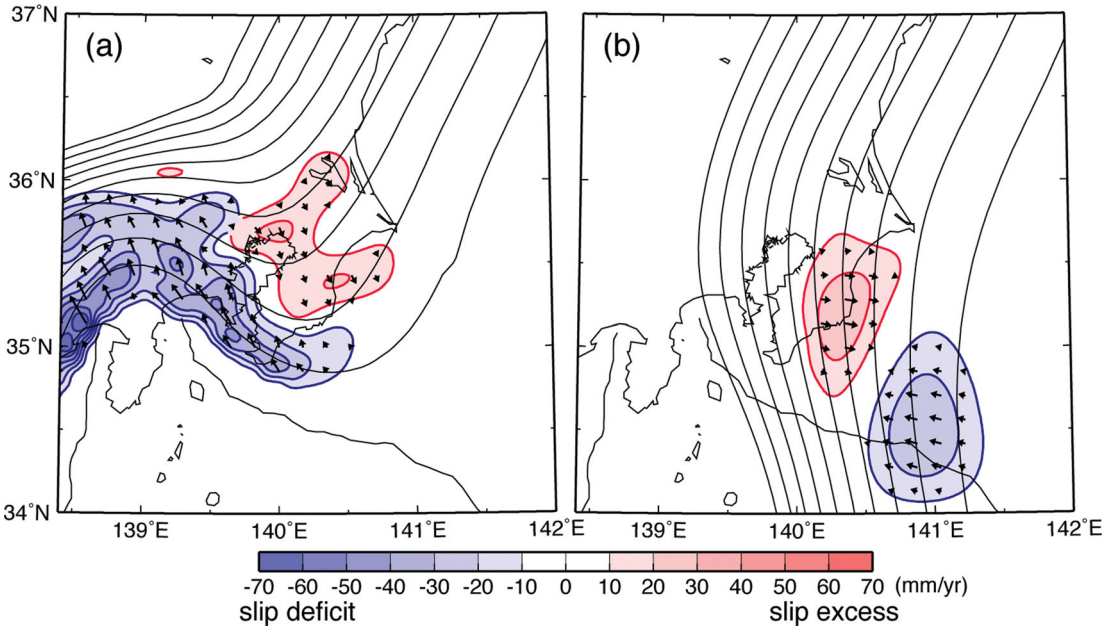

Figure 7. The interseismic slip-deficit rate distribution inverted from GPS strain rate data. (a) The NAM-PHS plate interface. (b) The PHS-PAC plate interface. The blue and red contours show slip-deficit and -excess rates at intervals of 10 mm yr^{-1}, respectively. The thick arrows indicate slip-rate vectors on each plate interface.

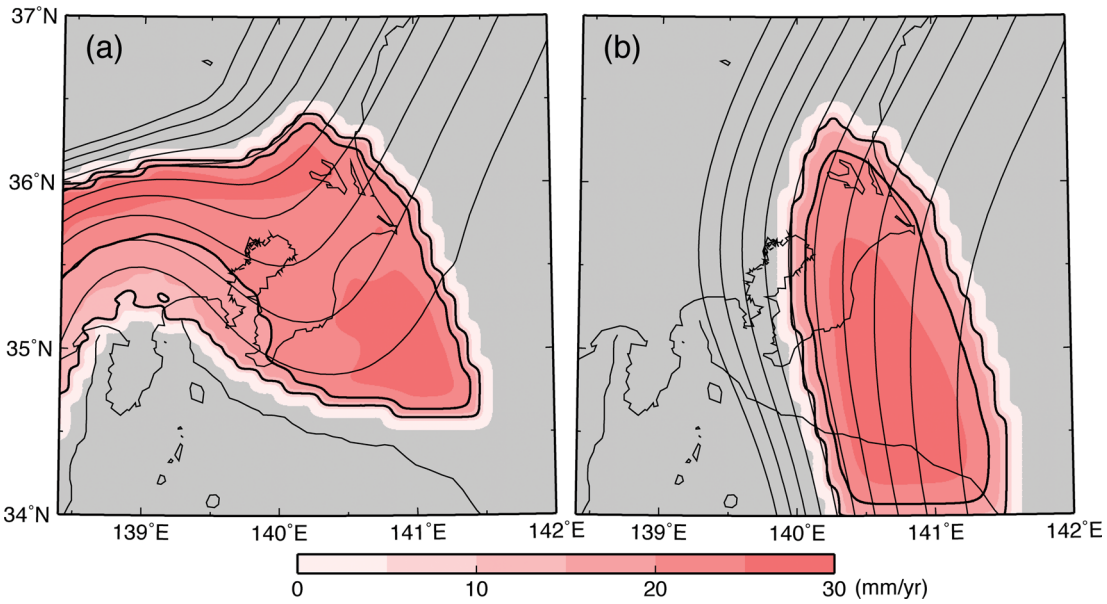

Figure 8. Estimation errors of the inverted slip-deficit rate distribution. (a) The NAM-PHS plate interface. (b) The PHS-PAC plate interface. The colour scale indicates the estimation errors. The contours are shown at 10 mm yr^{-1} intervals. The outsides of the model regions are coloured by grey. The errors are underestimated near the margins of the model regions.

in the present analysis, which cannot explain the intraplate inelastic deformation.

The inversion result for the PHS-PAC plate interface shown in Fig. 7(b) is not so reliable, because the estimation errors in Fig. 8(b) are almost the same magnitude as the peak values of slip-excess and -deficit rates. Nevertheless, the gentle slip-excess peak beneath the eastern part of the Boso peninsula and the gentle slip-deficit peak far southeast off the Boso peninsula seem to be significant. The slip-excess zone beneath the eastern part of the Boso peninsula might be related to ordinary high-seismic activity there. The slip-deficit zone far southeast off the Boso peninsula might correspond to the source region of the 1953 off Boso peninsula earthquake (M7.4).

For reference, we show the dilatation and maximum shear strain rates computed from the optimum slip-deficit rate distribution in Figs 9(a) and (b), respectively. The computed strain rates include the effects of slip deficit at both the NAM-PHS and PHS-PAC plate interfaces, but not the effects of steady plate subduction, which have been already subtracted from the original data. From the comparison of Figs 9(a) and (b) with Figs 5(a) and (b),

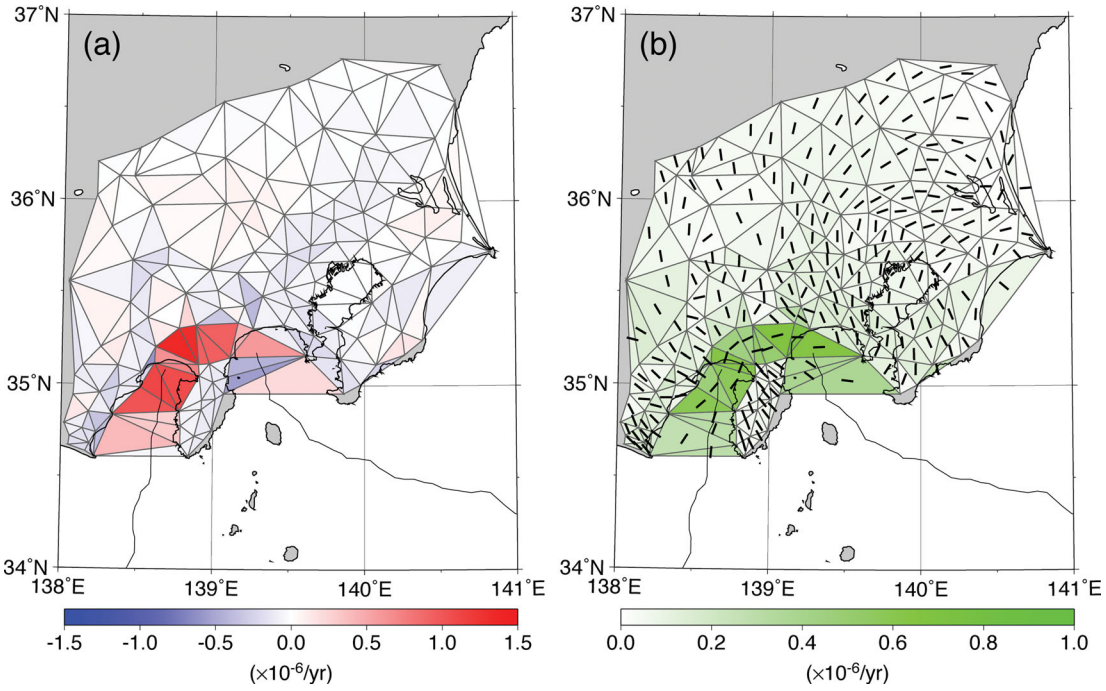

Figure 9. The horizontal strain rates computed from the inverted slip-deficit rate distribution. (a) Dilatation. (b) Maximum shear strain. The black bar in each triangle indicates the direction of maximum horizontal contraction. The grey solid lines show the optimum triangular mesh constructed from GPS stations with Delaunay triangulation.

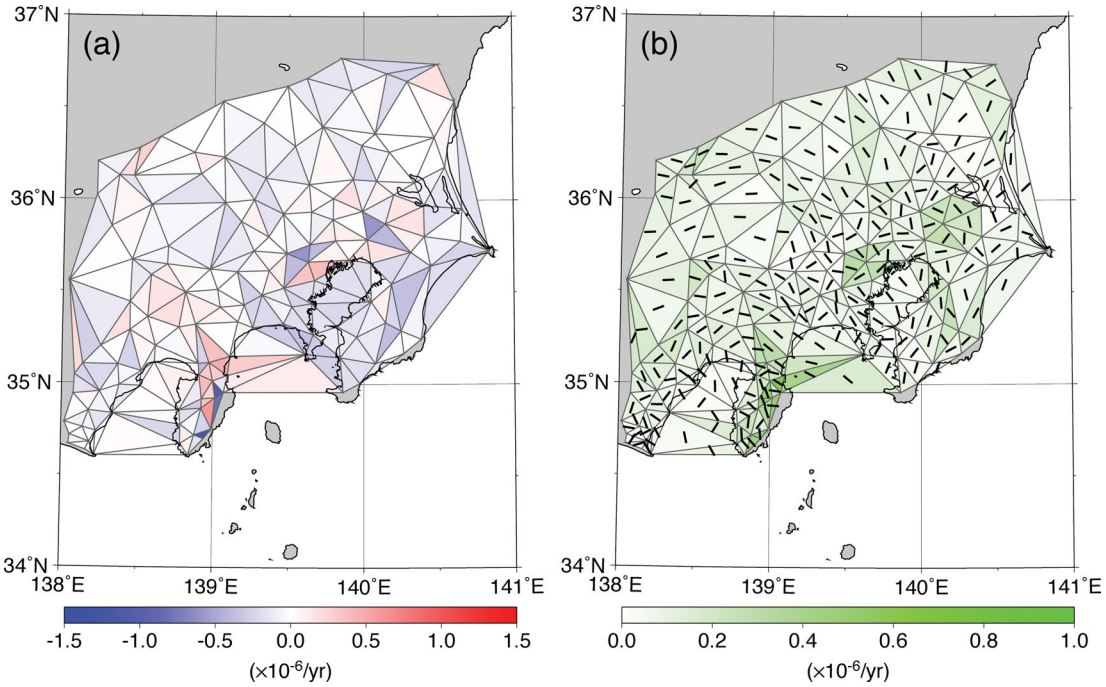

Figure 10. The residual strain rates obtained by subtracting the theoretical strain rates in Fig. 9 from the observed strain rates in Fig. 5. (a) Dilatation. (b) Maximum shear strain. The black bar in each triangle indicates the direction of maximum horizontal contraction. The grey solid lines show the optimum triangular mesh constructed from GPS stations with Delaunay triangulation.

respectively, we can see that the inverted slip-deficit rate distribution well explain the observed strain rates. In Fig. 10 we show also the residual strain rates, obtained by subtracting the theoretical strain rates in Fig. 9 from the observed strain rates in Fig. 5. The residual strain rates are incoherent except the Tokyo Bay area (central part of the Kanto region) covered by a thick sedimentary layer.

4 DISCUSSION

In Section 2.1, assuming the cyclic process of interseismic slip deficit and subsequent coseismic slip, we derived an approximate mathematical expression, eq. (14), for interseismic surface velocities due to slip deficit at plate interfaces. This expression is valid except the early stage of the earthquake cycle. In the early

postseismic period, as shown in eq. (13), we need to consider the effects of viscoelastic stress relaxation in the asthenosphere. From eq. (14), we can see that interseismic surface deformation is caused by not only steady slip-deficit increase in a seismogenic region but also steady slip motion over the whole plate interface. Furthermore, in the computation of interseismic surface deformation, we must use the completely relaxed displacement response, namely the response of an elastic plate floating on nonviscous liquid under gravity, to both the steady slip motion and slip-deficit increase. In most studies, however, the effects of steady slip motion at plate interfaces have been assumed to be zero, and the displacement response for elastic half-space have been used to slip-deficit increase as an approximation.

In the Kanto–Tokai region, Sagiya (1999, 2004) have estimated slip-deficit rate distribution on the Suruga and Sagami trough segments from the inversion analyses of GPS velocity data for 1997–1999 and 1996–2000, respectively. Henry *et al.* (2001) have also estimated the interseismic locking depths and coupling ratios of plate interfaces in central Japan, except the Izu–Mainland collision zone, from the inversion analysis of GPS strain data (1996–1998). As shown in Fig. 3(b), the steady subduction of the PHS plate beneath the NAM plate causes the large displacements of GPS stations relative to the Mainland in the Izu peninsula. In the analyses mentioned above, all the GPS data in the Izu peninsula have been discarded instead of considering the effects of steady plate subduction, and so they must have given up the estimation of slip-deficit rates in the Izu–Mainland collision zone. The data in the Izu peninsula are also crucial for the unbiased estimation of slip-deficit rate distribution on the Suruga and Sagami trough segments.

The relative motion of plates on the Earth's surface is generally described by rigid body rotation about a specific Euler pole. McCaffrey (2002) extended this idea to crustal block rotation and applied to the inversion of GPS velocity data to simultaneously estimate rigid block rotations and slip rates at block boundaries. Wallace *et al.* (2004) demonstrated the effectiveness of McCaffrey's approach through the inversion of GPS data in the North Island of New Zealand. The simultaneous GPS velocity data inversion for rigid block rotations and block-boundary slip rates will be applicable if the geometries of tectonic block boundaries are well defined as in the case of southwest Japan. In central Japan, however, the causes of rigid block rotations are not only the simple slip motion at specific tectonic boundaries (Taira *et al.* 1992) but also the brittle fracture and/or plastic flow at a number of defects spreading over indefinite tectonic boundary zones (Sagiya *et al.* 2000; Noda & Matsu'ura 2010). So, in this study, first, we calculated steady slip motion at plate interfaces from a global plate motion model (NUVEL1-A). Second, we computed the surface velocities due to the steady slip motion as shown in Fig. 3(b). Third, we subtracted the computed surface velocities from the observed GPS velocities in Fig. 3(a) to obtain the residual velocities in Fig. 3(c). Then, finally, we transformed the residual velocities into strain rates to remove the rigid translation and rotation of crustal blocks caused by inelastic deformation in ambiguous tectonic boundary zones.

To demonstrate the effectiveness of the displacement-strain transformation, we tried to directly solve the observation equation for residual velocities, eq. (23), with the same inversion formula and same prior information as used in the analysis of strain rates. The data errors $\mathbf{e}^{\mathrm{res}}$ in eq. (23) were simply assumed to be Gaussian with zero mean and covariance matrix $\sigma^2\mathbf{I}$, which means no correlation between the data errors. In Figs 11(a) and (b), we show the slip-deficit rate distribution on the NAM-PHS and PHS-PAC plate interfaces, respectively, estimated from the direct inversion of GPS velocity data with considering the rotation of the PHS plate relative to the NAM plate but not the block rotation of the Izu peninsula. From Fig. 11(a), we can find that a broad slip-deficit rate zone extends over the whole NAM-PHS plate interface with a ridge greater than 60 mm yr^{-1} parallel to the Sagami trough. From Fig. 11(b), we can also find a broad peak of high slip-excess rate (80 mm yr^{-1}) on the PHS-PAC plate interface. The 60-mm yr^{-1} slip-deficit rate on the NAM-PHS plate interface is too large in comparison with the steady subduction rate (30–40 mm yr^{-1}) of the PHS plate expected from a global plate motion model (NUVEL-1A). On the other hand, the slip-excess peak on the PHS-PAC plate interface might be explainable if a large slow-slip event occurred there during the observation period (1996–2000), but no such event has been reported. So, from a seismotectonic point of view, this inversion result is incomprehensible.

In Figs 12(a) and (b), we show the horizontal velocity fields reproduced from the results of GPS velocity data inversion (Fig. 11) and strain-rate data inversion (Fig. 7), respectively. These velocity fields include the effects of steady plate subduction in Fig. 3(b), and so we can directly compare them with the observed GPS velocity field in Fig. 3(a). From comparison of Figs 12(a) and (b) with Fig. 3(a), we can see that the observed GPS velocity data are well explained by the slip-deficit rate distribution inverted from velocity data but not that from strain-rate data. In Fig. 12(c), we show the residuals obtained by subtracting the velocities in Fig. 12(b) from those in Fig. 12(a) together with the tectonic boundaries in the Izu–Mainland collision zone (Taira *et al.* 1992). Here, the colour of triangular elements indicates the rotation rates, $\dot{\omega}_{12}$ in eq. (A2), calculated from the residual velocities, which should not be ascribed to interseismic slip deficit at plate interfaces. From theoretical consideration to rotation tensor in Appendix, we may ascribe the residual velocities mainly to rigid body translation and rotation of tectonic blocks; that is, the south-southeastward translation of the Izu microplate, which suggests plate convergence at the incipient subduction boundaries southeast off the Izu peninsula (Taira *et al.* 1992), the anticlockwise rotation of the south Kanto block, and the clockwise rotation of the Tokai block.

As pointed out by Yagi & Fukahata (2008), the proper setting of covariance matrices for data errors is crucial to obtain unbiased estimates in inversion analysis. The data errors generally consist of observation errors and modelling errors. In the case of GPS velocity data, we may suppose the observation errors to be Gaussian with zero mean and the covariance matrix $\sigma^2_{\mathrm{obs}}\mathbf{I}$. However, we have no reliable information about the modelling errors, which come from imperfection in theoretical models used for inversion analysis. In this study, we used a fairly sophisticated dislocation model considering the realistic 3-D geometry of plate interfaces and the viscoelasticity of the asthenosphere, but even then there remain some sources of modelling errors; rigid block translation and rotation, surface topography, sedimentary layer thickness and so on. Among them, the modelling errors due to rigid block translation and rotation have certainly long-range correlation, and so should be removed by transforming the GPS velocity data into strain rates. Since the modelling errors due to the remaining sources would have rather short-range correlation, we may suppose the covariance matrix $\sigma^2_{\mathrm{mod}}\mathbf{D}$ of them to be diagonal. So, on the assumption of no correlation between the observation errors and the modeling errors, we expressed the covariance matrix $\sigma^2\mathbf{E}$ of total data errors in the observation equation for GPS strain rates, eq. (24), in the form of eq. (30); that is $\sigma^2\mathbf{E} = \sigma^2(\mathbf{R}\mathbf{R}^{\mathrm{T}} + c^2\mathbf{D})$, where the first and second terms on the right side are the covariance matrices of observation

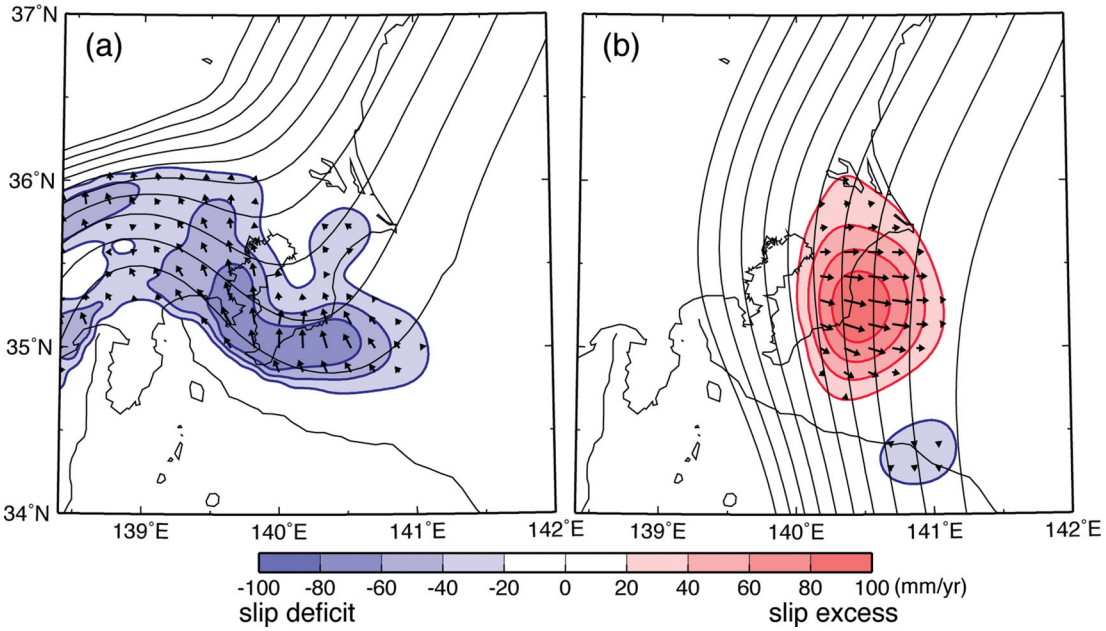

Figure 11. The slip-deficit rate distribution inverted from GPS velocity data on the assumption of no modelling errors. (a) The NAM-PHS plate interface. (b) The PHS-PAC plate interface. The blue and red contours show slip-deficit and -excess rates at intervals of 20 mm yr^{-1}, respectively. The thick arrows indicate slip-rate vectors on each plate interface.

errors and modelling errors, respectively, and c^2 is a parameter that controls the relative weight of modelling errors to observation errors.

In eq. (30) we can consider two extreme cases; that is $c^2 \to 0$ and $c^2 \to \infty$. In the first case, where the theoretical model is assumed to be perfect, the covariance matrix $\sigma^2\mathbf{E}$ tends to $\sigma^2\mathbf{R}\mathbf{R}^{\mathrm{T}}$. Since the matrix $\mathbf{R}\mathbf{R}^{\mathrm{T}}$ is not regular, we cannot use the inversion formulae in Section 2.4. However, the observation equation for GPS strain data, eq. (24), with the covariance matrix of $\sigma^2\mathbf{R}\mathbf{R}^{\mathrm{T}}$ is essentially the same as the observation equation for residual velocity data, eq. (23), with the covariance matrix of $\sigma^2\mathbf{I}$, and so the optimum solution in the case of $c^2 \to 0$ has been already given in Fig. 11. In the second case, where the modelling errors are much larger than the observation errors, the covariance matrix $\sigma^2\mathbf{E}$ tends to $\sigma^2c^2\mathbf{D}$. In this case, since the matrix $\mathbf{D}$ is regular, we can use the inversion formulae in Section 2.4. In Fig. 13, we show the solution in the case of $c^2 \to \infty$. The optimum slip-deficit rate distribution in Fig. 7 is significantly different from that in the first case ($c^2 \to 0$), but almost agrees with that in the second case ($c^2 \to \infty$). This means that the proper treatment of modelling errors is crucial in the analysis of interseismic GPS array data in the Kanto region.

In this study, we have not treated the vertical components of GPS velocity data. Although the observation errors of vertical components are much larger than those of horizontal components, they have also some information about crustal deformation due to interseismic slip-deficit rates at plate interfaces. We can easily incorporate the vertical components into the strain data inversion by transforming them to tilt rates, though mathematical formulation will become more complicated. However, the vertical components are essentially different from the horizontal components in terms of systematic errors. There exists an absolute reference (geoid) for vertical motion, but not for horizontal motion. Therefore, horizontal velocity data inevitably include some rigid body translation and rotation, which cause systematic errors as shown in this study. Another problem is the drastic change in thickness of the elastic lithosphere across island arcs. It would cause serious systematic errors in theoretical response functions for vertical deformation, but not for horizontal deformation, because the gravitational effect of flattening an elastic plate strongly depends on its thickness. Thus, for successful joint inversion of the vertical and horizontal components of interseismic GPS array data, we need to resolve the problem of systematic errors in vertical response functions.

5 CONCLUSIONS

In Section 2, assuming the cyclic process of interseismic slip deficit and subsequent coseismic slip in seismogenic regions at a plate interface, we obtained a theoretical expression to compute interseismic surface velocities for given slip-deficit rate distribution, which clearly shows that interseismic crustal deformation is caused by not only slip-deficit increase in seismogenic regions but also steady slip motion over the whole plate interface. On the basis of this theoretical expression, we developed an inversion method to estimate unbiased interseismic slip-deficit rates at plate interfaces from observed GPS velocity data in the framework of Bayesian statistical inference theory. In this method, first, we subtract theoretical surface velocities due to known steady relative plate motion from the observed GPS data, and presume the residuals to be caused by slip deficit at plate interfaces. However, the observed GPS data always include rigid block translation and rotation, which cannot be explained by the slip-deficit model based on elastic dislocation theory. We treated the rigid block translation and rotation as systematic errors in the analysis, and removed them by transforming the velocity data into the average strain rates of triangle elements composed of adjacent GPS stations. In Section 3, we demonstrated the applicability of the strain data inversion method through the analysis of interseismic GPS velocity data (1996–2000) in the Kanto region, central Japan, where the NAM, PAC and PHS plates are interacting with each other in a complicated way. From this analysis, we found a broad and high slip-deficit rate zone on the NAM-PHS plate interface, extending from southeast off the Boso peninsula to the

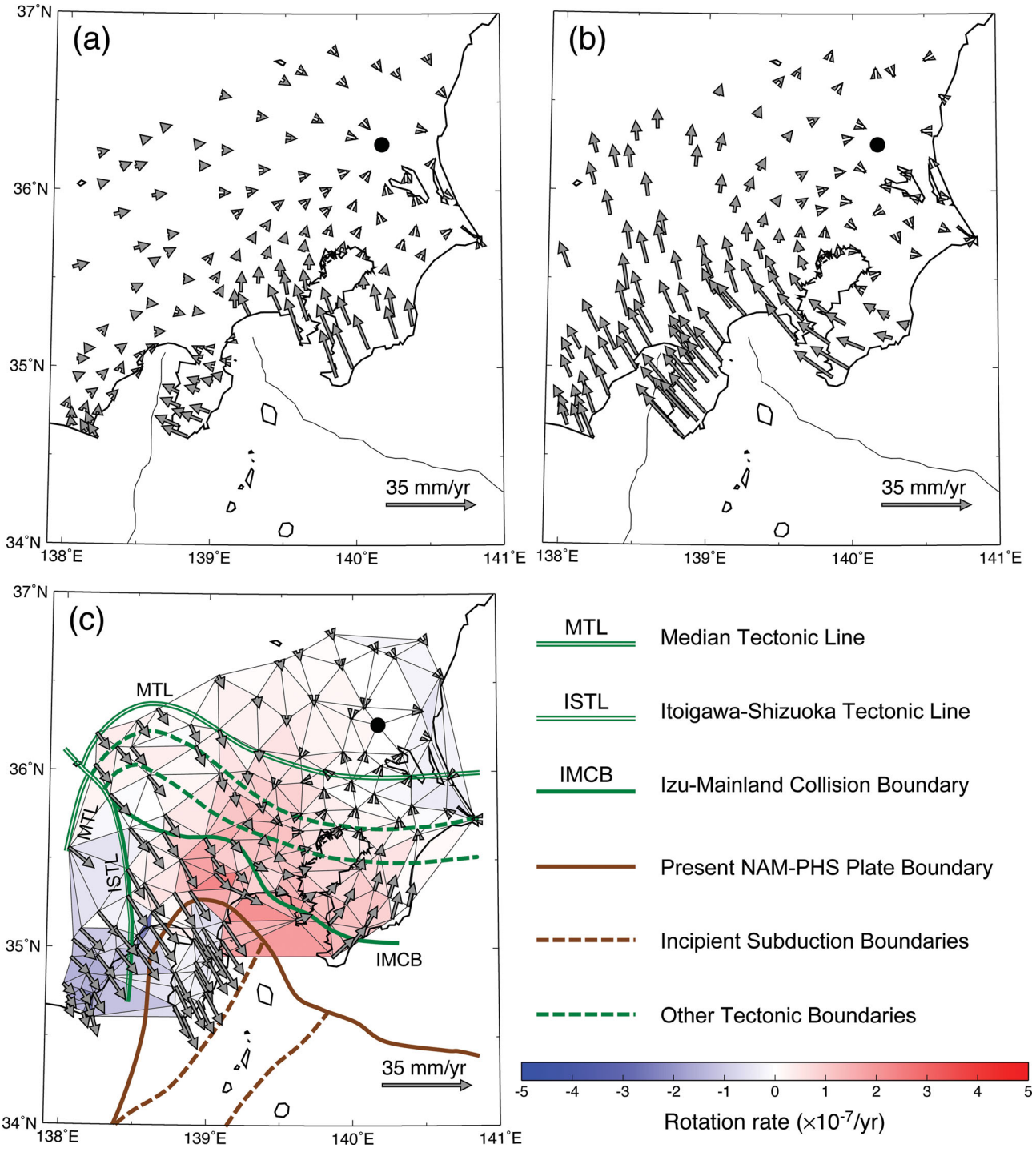

Figure 12. Comparison of the horizontal velocity fields reproduced from the two inversion results. (a) The velocity field reproduced from the result of GPS velocity data inversion in Fig. 11. (b) The velocity field reproduced from the result of GPS strain-rate data inversion in Fig. 7. In either case of (a) and (b), the reproduced velocity field includes the effect of steady plate subduction. The solid circle indicates a reference point (YST) to represent velocity vectors. (c) Difference between the velocity fields in (a) and (b). The colour of triangle elements indicates the rotation rates calculated from the residual velocities. The coloured thick lines are tectonic boundaries in the Izu-Mainland collision zone (Taira *et al.* 1992).

Tokai region through the Izu–Mainland collision zone. Two high slip-deficit rate zones along the Sagami and Suruga troughs correspond to the source regions of the 1923 Kanto earthquake (M7.9) and a potential Tokai earthquake, respectively. On the PHS-PAC plate interface, though the estimation errors are large, we found a moderate slip-deficit rate zone far southeast off the Boso peninsula, where an M7.4 earthquake has occurred in 1953.

ACKNOWLEDGMENTS

We thank Takeshi Sagiya for permitting us to use GPS velocity data (1996–2000) in the Kanto region, central Japan. We thank also Bert Vermeersen, Duncan Agnew, John Beavan and anonymous reviewers for their useful comments and suggestions to improve our manuscript. Computation for viscoelastic slip-response functions

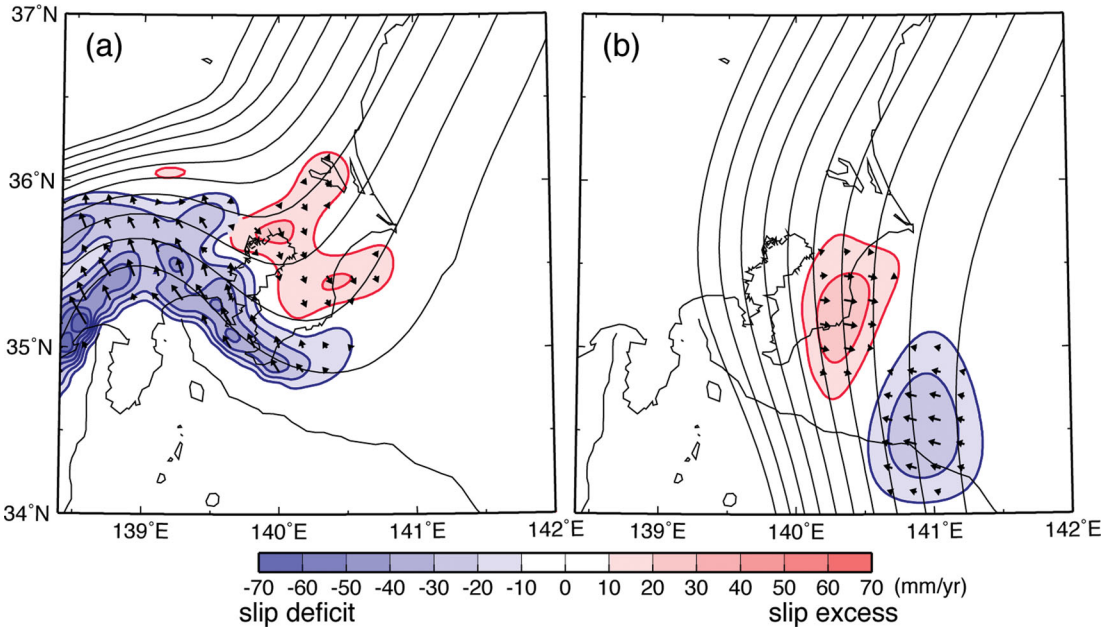

Figure 13. The slip-deficit rate distribution inverted from GPS strain rate data on the assumption of no observation errors. (a) The NAM-PHS plate interface. (b) The PHS-PAC plate interface. The blue and red contours show slip-deficit and -excess rates at intervals of 10 mm yr^{-1}, respectively. The thick arrows indicate slip-rate vectors on each plate interface.

was carried out with a supper-parallel computer at the Earth Simulator Center, JAMSTEC. Computation for GPS strain data inversion was carried out with a super computer at the Earthquake Research Institute, the University of Tokyo.

REFERENCES

Akaike, H., 1977. On entropy maximization principle, in *Application of Statistics,* pp. 27–41, ed. Krishnaiah, P.R., North-Holland, Amsterdam.

Akaike, H., 1980. Likelihood and the Bayes procedure, in *Bayesian Statistics,* pp. 143–166, eds Bernardo, J.M., DeGroot, M.H., Lindley, D.V. & Smith, A.F.M., University Press, Valencia.

Backus, G. & Mulcahy, M., 1976a. Moment tensors and other phenomenological descriptions of seismic sources–I. Continuous displacements, *Geophys. J. R. astr. Soc.,* **46,** 341–361.

Backus, G. & Mulcahy, M. 1976b. Moment tensors and other phenomenological descriptions of seismic sources–II. Discontinuous displacements, *Geophys. J. R. astr. Soc.,* **47,** 301–329.

Cathles, L.M., 1975. *The Viscosity of the Earth's Mantle,* Princeton University Press, Princeton, New Jersey.

De Berg, M., van Kreveld, M., Overmars, M. & Schwarzkopf, O., 1997. *Computational Geometry: Algorithm and Applications,* pp. 191–218, Springer-Verlag, Berlin, Heidelberg.

DeMets, C., Gordon, R.G., Argus, D.F. & Stein, S., 1994. Effect of recent revisions to the geomagnetic reversal time scale on estimates of current plate motions, *Geophys. Res. Lett.,* **21,** 2191–2194.

Feigl, K.L., King, R.W. & Jordan, T.H., 1990. Geodetic measurement of tectonic deformation in the Santa Maria fold and thrust belt, California, *J. geophys. Res.,* **95,** 2679–2699.

Fukahata, Y. & Matsu'ura, M., 2006. Quasi-static internal deformation due to a dislocation source in a multilayered elastic/viscoelastic half-space and an equvalence theorem, *Geophys. J. Int.,* **166,** 418–434.

Fukahata, Y., Nishitani, A. & Matsu'ura, M., 2004. Geodetic data inversion using ABIC to estimate slip history during one earthquake cycle with viscoelastic slip-response functions, *Geophys. J. Int.,* **156,** 140–153.

Fung, Y.C., 1965. *Foundations of Solid Mechanics,* Prentice-Hall, Englewood Cliffs, New Jersey, pp. 99–103.

Hashima, A., Takada, Y., Fukahata, Y. & Matsu'ura, M., 2008. General expressions for internal deformation due to a moment tensor in an elastic/viscoelastic multilayered half-space, *Geophys. J. Int.,* **175,** 992–1012.

Hashimoto, C., Fukui, K. & Matsu'ura, M., 2004. 3-D modeling of plate interfaces and numerical simulation of long-term crustal deformation in and around Japan, *Pure appl. geophys.,* **161,** 2053–2068.

Hashimoto, C., Noda, A., Sagiya, T. & Matsu'ura, M., 2009. Interplate seismogenic zones along the Kuril-Japan trench inferred from GPS data inversion, *Nat. Geosci.,* **2,** 141–144.

Hashimoto, C., Noda, A. & Matsu'ura, M., 2012. The Mw9.0 northeast Japan earthquake: total rupture of a basement asperity, *Geophys. J. Int.,* **189,** 1–5.

Hatori, T., 1976. Documents of tsunami and crustal deformation in Tokai District associated with the Ansei earthquake of Dec. 23, 1854, *Bull. Earthq. Res. Inst., Univ. Tokyo,* **51,** 13–28 (in Japanese with English abstract).

Hatori, T., 1977. Field investigation of the Tokai tunamis in 1707 and 1854 along the Shizuoka coast, *Bull. Earthq. Res. Inst., Univ. Tokyo,* **52,** 407–439 (in Japanese with English abstract).

Henry, P., Mazzotti, S. & Le Pichon, X., 2001. Transient and permanent deformation of central Japan estimated by GPS 1. Interseismic loading and subduction kinematics, *Earth planet. Sci. Lett.,* **184,** 443–453.

Hirose, F., Nakajima, J. & Hasegawa, A., 2008. A three-dimensional velocity structure and configuration of the Philippine Sea slab beneath Kanto district, central Japan, estimated by double-difference tomography, *J. seism. Soc. Japan,* **60,** 123–138 (in Japanese with English abstract).

Ishibashi, K., 1981. Specification of a soon-to-occur seismic faulting in the Tokai district, central Japan, based upon seismotectonics, in *Earthquake Prediction: An International Review, Maurice Ewing Series,* Vol. 4, pp. 297–332, eds Simpson, D.W. & Richards, P.G., AGU, Washington, DC.

Ishida, M., 1992. Geometry and relative motion of the Philippine Sea plate and Pacific plate beneath the Kanto-Tokai district, Japan, *J. geophys. Res.,* **97,** 489–513.

Ito, T., Yoshioka, S. & Miyazaki, S., 1999. Interplate coupling in southwest Japan deduced from inversion analysis of GPS data, *Phys. Earth planet. Inter.,* **115,** 17–34.

Ito, T., Yoshioka, S. & Miyazaki, S., 2000. Interplate coupling in northeast Japan deduced from inversion analysis of GPS data, *Earth planet. Sci. Lett.,* **176,** 117–130.

Jackson, D.D. & Matsu'ura, M., 1985. A Bayesian approach to nonlinear inversion, *J. geophys. Res.,* **90,** 581–591.
Knopoff, L., 1958. Energy release in earthquakes, *Geophys. J. R. astr. Soc.,* **1,** 44–52.
McCaffrey, R., 2002. Crustal block rotations and plate coupling, in *Plate Boundary Zones, Geodynamics Ser.,* Vol. 30, pp. 100–122, eds Stein, S. & Freymueller, J., AGU, Washington, DC.
Matsuda, T., 1977. Estimation of future destructive earthquakes from active faults on land in Japan, *J. Phys. Earth,* **25**(Suppl.), S251–S260.
Matsu'ura, M. & Iwasaki, T., 1983. Study on coseismic and postseismic crustal movements associated with the 1923 Kanto earthquake, *Tectonophysics,* **97,** 201–215.
Matsu'ura, M., Jackson, D.D. & Cheng, A., 1986. Dislocation model for aseismic crustal deformation at Hollister, California, *J. geophys. Res.,* **91,** 12 661–12 674.
Matsu'ura, M., Noda, A. & Fukahata, Y., 2007. Geodetic data inversion based on Bayesian formulation with direct and indirect prior information, *Geophys. J. Int.,* **171,** 1342–1351.
Matsu'ura, M. & Sato, T., 1989. A dislocation model for the earthquake cycle at convergent plate boundaries, *Geophys. J. Int.,* **96,** 23–32.
Mazzotti, S., Le Pichon, X., Henry, P. & Miyazaki, S., 2000. Full interseismic locking of the Nankai and Japan-west Kurile subduction zones: an analysis of uniform elastic strain accumulation in Japan constrained by permanent GPS, *J. geophys. Res.,* **105,** 13 159–13 177.
Nakajima, J. & Hasegawa, A., 2006. Anomalous low-velocity zone and linear alignment of seismicity along it in the subducted Pacific slab beneath Kanto, Japan: reactivation of subducted fracture zone? *Geophys. Res. Lett.,* **33,** L16309, doi:10.1029/2006GL026773.
Nakajima, J. & Hasegawa, A., 2007. Subduction of the Philippine Sea plate beneath southwestern Japan: slab geometry and its relationship to arc magmatism, *J. geophys. Res.,* **112,** B08306, doi:10.1029/2006JB004770.
Nishimura, T., 2002. Earthquake triggering due to volcanic deformation sources in areas east off Ito and around the Mt. Iwate volcano, *J. Geogr.,* **111,** 166–174 (in Japanese with English abstract).
Nishimura, T., Hirasawa, T., Miyazaki, S., Sagiya, T., Tada, T., Miura, S. & Tanaka, K., 2004. Temporal change of interplate coupling in northeast Japan during 1995–2002 estimated from continuous GPS observations, *Geophys. J. Int.,* **57,** 901–916.
Nishimura, T., Sagiya, T. & Stein, R.S., 2007. Crustal block kinematics and seismic potential of the northernmost Philippine Sea plate and Izu microplate, central Japan, inferred from GPS and leveling data, *J. geophys. Res.,* **112,** B005414, doi:10.1029/2005JB004102.
Noda, A. & Matsu'ura, M., 2010. Physics-based GPS data inversion to estimate 3-D elastic and inelastic strain fields, *Geophys. J. Int.,* **182,** 513–530.
Prescott, W.H., Savage, J.C. & Kinoshita, W.T., 1979. Strain accumulation rates in the western United States between 1970–1978, *J. geophys. Res.,* **84,** 5423–5435.
Sagiya, T., 1999. Interplate coupling in the Tokai district, central Japan, deduced from continuous GPS data, *Geophys. Res. Lett.,* **26,** 2315–2318.
Sagiya, T., 2004. Interplate coupling in the Kanto district, central Japan, and the Boso peninsula silent earthquake in May 1996, *Pure appl. geophys.,* **161,** 2327–2342.
Sagiya, T., Miyazaki, S. & Tada, T., 2000. Continuous GPS array and present-day crustal deformation of Japan, *Pure appl. Geophys.,* **157,** 2303–2322.
Sato, T. & Matsu'ura, M., 1992. Cyclic crustal movement, steady uplift of marine terraces, and evolution of the island arc-trench system in southwest Japan, *Geophys. J. Int.,* **111,** 617–629.
Savage, J.C., 1969. Steketee's paradox, *Bull. seism. Soc. Am.,* **59,** 381–384.
Savage, J.C., 1983. A dislocation model of strain accumulation and release at a subduction zone, *J. geophys. Res.,* **88,** 4984–4996.
Savage, J.C. & Prescott, W.H., 1978. Asthenosphere readjustment and the earthquake cycle, *J. geophys. Res.,* **83,** 3369–3376.
Spence, D.A. & Turcotte, D.L., 1979. Viscoelastic relaxation of cyclic displacements on the San Andreas fault, *Proc. R. Soc. A.,* **365,** 121–144.
Suwa, Y., Miura, S., Hasegawa, A., Sato, T. & Tachibana, K., 2006. Interplate coupling beneath NE Japan inferred from three-dimensional displacement field, *J. geophys. Res.,* **111,** B04402, doi:10.1029/2004JB003203.
Taira, A., Pickering, K.T., Windley, B.F. & Soh, W., 1992. Accretion of Japanese Island arcs and implications for the origin of Archean greenstone belts, *Tectonics,* **11,** 1224–1244.
Terakawa, T. & Matsu'ura, M., 2010. The 3-D tectonic stress fields in and around Japan inverted from centroid moment tensor data of seismic events, *Tectonics,* **29,** TC6008, doi:10.1029/2009TC002626.
Tsuboi, C., 1932. Investigation on the deformation of the earth's crust in Idu peninsula connected with the Idu earthquake of Nov. 26, 1930, *Bull. Earthq. Res. Inst., Univ. Tokyo,* **10,** 435–448.
Wallace, L.M., Beavan, J., McCaffrey, R. & Darby, D., 2004. Subduction zone coupling and tectonic block rotations in the North Island, New Zealand, *J. geophys. Res.,* **109,** B12406, doi:10.1029/2004JB003241.
Yabuki, T. & Matsu'ura, M., 1992. Geodetic data inversion using a Bayesian information criterion for spatial distribution of fault slip, *Geophys. J. Int.,* **109,** 363–375.
Yagi, Y. & Fukahata, Y., 2008. Importance of covariance components in inversion analyses of densely sampled observed data: an application to waveform data inversion for seismic source processes, *Geophys. J. Int.,* **175,** 215–221.
Yoshioka, S., Yabuki, T., Sagiya, T., Tada, T. & Matsu'ura, M., 1993. Interplate coupling and relative plate motion in the Tokai district, central Japan, deduced from geodetic data inversion using ABIC, *Geophys. J. Int.,* **113,** 607–621.
Yoshioka, S., Yabuki, T., Sagiya, T., Tada, T. & Matsu'ura, M., 1994. Interplate coupling in the Kanto district, central Japan, deduced from geodetic data and its tectonic implications, *Tectonophysics,* **229,** 181–200.

APPENDIX: ELIMINATING SYSTEMATIC ERRORS FROM GPS ARRAY DATA

Through GPS measurements we can determine the current coordinates of observation points in a geodetic reference frame. The GPS displacement data, which are the difference between the current and previous coordinates of observation points, contain not only intrinsic deformation but also rigid block translation and rotation, which cannot be explained by the slip-deficit models based on elastic dislocation theory. If observed data contain theoretically unexplainable coherent noise (systematic errors), the result of inversion analysis will be seriously biased. So, we need to remove the rigid block translation and rotation from GPS displacement data.

Representation of displacement fields in terms of strain

We consider the horizontal deformation of the Earth's surface. As geodetic reference frame, we take a Cartesian coordinate system (x_1, x_2, x_3) with the x_3-axis pointing vertically upward. Then the displacement field within a crustal block Ω is represented as

$$u_i(\mathbf{x}) = u_i'(\mathbf{x}) + c_i \quad (i = 1, 2), \tag{A1}$$

where the constant c_i denotes the x_i-component of rigid body translation of the block. The displacement gradients $\partial u_i/\partial x_j$ are independent of the rigid body translation, and can be written in terms of the strain tensor ε_{ij} and the rotation tensor ω_{ij}, defined by

$$\varepsilon_{ij} = \frac{1}{2}\left(\frac{\partial u_i}{\partial x_j} + \frac{\partial u_j}{\partial x_i}\right) \quad \text{and}$$
$$\omega_{ij} = \frac{1}{2}\left(\frac{\partial u_j}{\partial x_i} - \frac{\partial u_i}{\partial x_j}\right) \quad (i = 1, 2; \quad j = 1, 2), \tag{A2}$$

respectively, as

$$\frac{\partial u_i}{\partial x_j} = \varepsilon_{ij} - \omega_{ij} \quad (i = 1, 2; j = 1, 2). \tag{A3}$$

If the displacement u_i^0 and rotation ω_{ij}^0 $(= -\omega_{ji}^0)$ of a fiducial point P_0 at $\mathbf{x} = \mathbf{x}^0$ in Ω are known, the displacement u_i^k of an arbitrary point P_k at $\mathbf{x} = \mathbf{x}^k$ in Ω are represented by the following line integral along an arbitrary path connecting P_0 and P_k:

$$u_i^k = u_i^0 + \int_{P_0}^{P_k} \frac{\partial u_i}{\partial x_j} \mathrm{d}x_j = u_i^0 + \int_{P_0}^{P_k} \varepsilon_{ij} \mathrm{d}x_j - \int_{P_0}^{P_k} \omega_{ij} \mathrm{d}x_j \quad (i = 1, 2). \tag{A4}$$

Now we divide the rotation tensor $\omega_{ij}(\mathbf{x})$ into a spatially variable part $\omega'_{ij}(\mathbf{x})$ and a spatially constant part γ_{ij}:

$$\omega_{ij}(\mathbf{x}) = \omega'_{ij}(\mathbf{x}) + \gamma_{ij} \quad (i = 1, 2; j = 1, 2). \tag{A5}$$

According to Fung (1965, Section 4.6), the rotation tensor ω_{ij} is generally related with the strain tensor ε_{ij} by the following equation:

$$\frac{\partial \omega_{ij}}{\partial x_\alpha} = \frac{\partial \varepsilon_{j\alpha}}{\partial x_i} - \frac{\partial \varepsilon_{i\alpha}}{\partial x_j} \quad (i = 1, 2; j = 1, 2; \alpha = 1, 2). \tag{A6}$$

Then, substituting eq. (A5) into the above equation, we obtain

$$\frac{\partial \omega'_{ij}}{\partial x_\alpha} = \frac{\partial \varepsilon_{j\alpha}}{\partial x_i} - \frac{\partial \varepsilon_{i\alpha}}{\partial x_j} \quad \text{and} \quad \frac{\partial \gamma_{ij}}{\partial x_\alpha} = 0. \tag{A7}$$

That is, the spatially variable part ω'_{ij} of rotation tensor is a function of strain, but the spatially constant part γ_{ij} is independent of strain. The rigid body rotation of the block Ω is realized if $\varepsilon_{ij}(\mathbf{x}) = 0$ and $\omega_{ij}(\mathbf{x}) = \gamma_{ij}$ over Ω, and so we call γ_{ij} $(= -\gamma_{ji})$ rigid block rotation hereafter. On the other hand, ω'_{ij} should be called intrinsic rotation.

Substituting eq. (A5) into eq. (A4),

$$u_i^k = u_i^0 - (x_j^k - x_j^0)\gamma_{ij} + \int_{P_0}^{P_k} \varepsilon_{ij} \mathrm{d}x_j - \int_{P_0}^{P_k} \omega'_{ij} \mathrm{d}x_j, \tag{A8}$$

integrating the last term on the right side of the above equation by parts,

$$u_i^k = u_i^0 - (x_j^k - x_j^0)(\omega_{ij}'^0 + \gamma_{ij}) + \int_{P_0}^{P_k} \varepsilon_{ij} \mathrm{d}x_j + \int_{P_0}^{P_k} \frac{\partial \omega'_{ij}}{\partial x_\alpha}(x_j - x_j^k)\, \mathrm{d}x_\alpha, \tag{A9}$$

and eliminating ω'_{ij} in terms of ε_{ij} with eq. (A7), we finally obtain

$$u_i^k = u_i^0 - (x_j^k - x_j^0)\omega_{ij}^0 + \int_{P_0}^{P_k} U_{i\alpha}(\mathbf{x})\, \mathrm{d}x_\alpha \quad (i = 1, 2) \tag{A10}$$

with

$$u_i^0 = u_i'^0 + c_i \quad (i = 1, 2), \tag{A11}$$

$$\omega_{ij}^0 = \omega_{ij}'^0 + \gamma_{ij} \quad (i = 1, 2; j = 1, 2), \tag{A12}$$

and

$$U_{i\alpha}(\mathbf{x}) = \varepsilon_{i\alpha}(\mathbf{x}) + (x_j^k - x_j)\left(\frac{\partial \varepsilon_{i\alpha}(\mathbf{x})}{\partial x_j} - \frac{\partial \varepsilon_{j\alpha}(\mathbf{x})}{\partial x_i}\right) \quad (i = 1, 2; \alpha = 1, 2). \tag{A13}$$

If the fiducial point is located at some place with no intrinsic deformation ($u_i'^0 = 0$ and $\omega_{ij}'^0 = 0$), the above representation of displacement field (Fung 1965, Section 4.6) becomes

$$u_i^k = c_i - (x_j^k - x_j^0)\gamma_{ij} + \int_{P_0}^{P_k} U_{i\alpha}(\mathbf{x})\, \mathrm{d}x_\alpha \quad (i = 1, 2). \tag{A14}$$

That is, the effects of rigid block translation (c_i) and rotation (γ_{ij}) on the displacement field cannot be eliminated even if we choose the fiducial point at some place with no intrinsic deformation.

We consider the case in which the fiducial point P_0 is in a crustal block Ω_1 and the target point P_k is in another contiguous crustal block Ω_2. In such a case, neglecting intrinsic deformation at P_0 for simplicity, we can represent the displacement at P_k by the following line integral along a path crossing the block boundary at a point P_b:

$$u_i^k = c_i^1 - (x_j^{b-} - x_j^0)\gamma_{ij}^1 + \int_{P_0}^{P_b^-} U_{i\alpha}(\mathbf{x})\, \mathrm{d}x_\alpha + \Delta u_i^b - (x_j^k - x_j^{b+})\gamma_{ij}^2 + \int_{P_b^+}^{P_k} U_{i\alpha}(\mathbf{x})\, \mathrm{d}x_\alpha. \tag{A15}$$

Here, c_i^1 and γ_{ij}^1 are the rigid body translation and rotation of the block Ω_1, γ_{ij}^2 is the rigid body rotation of the block Ω_2, and Δu_i^b denotes the offset at the block boundary. In a similar way, we can easily extend the path integral representation of displacement field to multiblock cases.

Elimination of systematic errors from GPS array data

As can be seen from eq. (A10), the displacement u_i^k $(i = 1, 2)$ of an arbitrary point P_k depends on the unknown displacement u_i^0 $(i = 1, 2)$ and rotation ω_{12}^0 $(= -\omega_{21}^0)$ of a fiducial point P_0. A serious problem is that the effects of rotation ω_{12}^0 increase with the distance from the fiducial point. Now we consider a triangle $\Delta P_k P_l P_m$ composed of GPS observation points, P_k, P_l and P_m, as shown in Fig. A1, where P_0 indicates a fiducial point. Then, we obtain similar expressions to eq. (A10) for the points P_l and P_m. First, we eliminate the translation term u_i^0 by taking the difference between u_i^k and u_i^l:

$$\begin{cases} u_1^l - u_1^k = -\sin\theta_{kl} l_{kl} \omega_{12}^0 + \int_{P_k}^{P_l} U_{11}\, \mathrm{d}x_1 + \int_{P_k}^{P_l} U_{12}\, \mathrm{d}x_2 \\ u_2^l - u_2^k = \cos\theta_{kl} l_{kl} \omega_{12}^0 + \int_{P_k}^{P_l} U_{21}\, \mathrm{d}x_1 + \int_{P_k}^{P_l} U_{22}\, \mathrm{d}x_2 \end{cases}, \tag{A16}$$

where l_{kl} and θ_{kl} denote the side length $\overline{P_k P_l}$ and its direction measured from the x_1-axis, respectively. Next, we rotate the coordinate system (x_1, x_2, x_3) around the x_3-axis by θ_{kl} anticlockwise so that the x_1-axis points to the direction of $\overline{P_k P_l}$. In the new coordinate

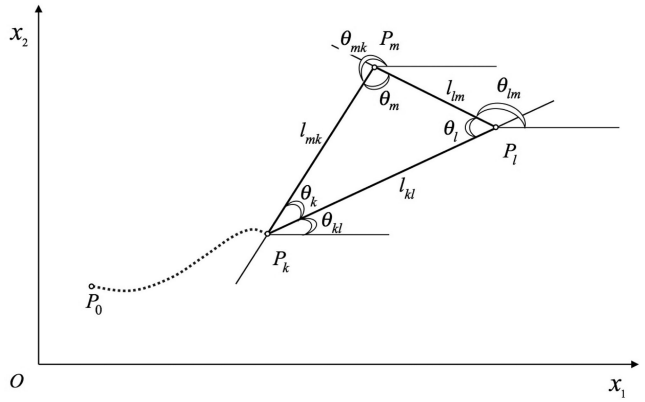

Figure A1. Notation for the side lengths and angles of a triangle composed of GPS stations. l_{ij}: The length of a side $\overline{P_i P_j}(ij = kl, lm, mk)$. θ_{ij}: The angle between a side $\overline{P_i P_j}$ and the x_1-axis. θ_i: The internal angle at a vertex P_i $(i = k, l, m)$. The dotted line indicates a path connecting the fiducial point P_0 and an arbitrary point P_k.

system (x_1', x_2', x_3), assuming locally homogeneous strain, eq. (A16) can be written as

$$\begin{cases} u_1'^l - u_1'^k = \int_{P_k}^{P_l} U_{11}' \mathrm{d}x_1' \cong l_{kl} \bar{\varepsilon}_{11}'^{kl} \\ u_2'^l - u_2'^k = l_{kl}\omega_{12}^0 + \int_{P_k}^{P_l} U_{21}' \mathrm{d}x_1' \cong l_{kl}[\omega_{12}^0 + \bar{\varepsilon}_{12}'^{kl}] \end{cases}, \tag{A17}$$

where $\bar{\varepsilon}_{11}'^{kl}$ and $\bar{\varepsilon}_{12}'^{kl}$ represent the average of ε_{11}' and ε_{12}' over $\overline{P_k P_l}$, respectively. From eq. (A17) we can see that the x_1'-component of the relative displacement vector (side-length change) gives simple extension $\bar{\varepsilon}_{11}'^{kl}$ in the new coordinate system. On the other hand, the x_2'-component gives the inseparable composite of simple shear $\bar{\varepsilon}_{12}'^{kl}$ and rotation ω_{12}^0 (Noda & Matsu'ura 2010).

In the analysis of GPS displacement data, we use only the x_1'-components, which correspond to the baseline-length changes in trilateration. Instead of discarding the x_2'-components, we combine the changes of three side lengths Δl_{ij} $(ij = kl, lm, mk)$ for the triangle $\Delta P_k P_l P_m$ to get complete information about its intrinsic deformation, which can be written in the original coordinate system as

$$\begin{aligned} \Delta l_{ij} = &-\cos\theta_{ij} u_1^i - \sin\theta_{ij} u_2^i \\ &+ \cos\theta_{ij} u_1^j + \sin\theta_{ij} u_2^j \quad (ij = kl, lm, mk). \end{aligned} \tag{A18}$$

In fact, given the side-length changes, we can determine three horizontal strain components uniquely (e.g. Tsuboi 1932; Prescott *et al.* 1979; Feigl *et al.* 1990).

After eliminating the systematic errors due to rigid block translation and rotation, the observed data (side-length changes) still contain the theoretically unexplainable deformation caused by brittle fracture and/or plastic flow at a number of defects in the Earth's crust. The effects of theoretically unexplainable deformation are cumulative and have long-range correlation in displacements as shown in eq. (A10), but not in side-length changes as shown in eq. (A17). Therefore, using side-length changes as data instead of displacements, we can treat them as random errors in the analysis.

Transformation of displacement data into strains

On the assumption of locally homogeneous strain, Tsuboi (1932) first obtained the explicit transformation formula from the horizontal displacement components, u_1^j and u_2^j, at the vertexes P_j $(j = k, l, m)$ of a triangle $\Delta P_k P_l P_m$ into its horizontal strain components, ε_{11}^{klm}, ε_{12}^{klm} and ε_{22}^{klm}. We can rewrite his formula in a more convenient form for error analysis:

$$\begin{pmatrix} \varepsilon_{11}^{klm} \\ \varepsilon_{12}^{klm} \\ \varepsilon_{22}^{klm} \end{pmatrix} = \mathbf{A}_{klm} \mathbf{B}_{klm} \begin{pmatrix} u_1^k \\ u_2^k \\ u_1^l \\ u_2^l \\ u_1^m \\ u_2^m \end{pmatrix}, \tag{A19}$$

where $\mathbf{A}_{klm}$ and $\mathbf{B}_{klm}$ are the matrices defined by

$$\mathbf{A}_{klm} = \frac{1}{l_{kl} l_{lm} l_{mk} s_k s_l s_m} \times \begin{bmatrix} -l_{lm} l_{mk} s_{lm} s_{mk} s_m & -l_{mk} l_{kl} s_{mk} s_{kl} s_k & -l_{kl} l_{lm} s_{kl} s_{lm} s_l \\ \frac{1}{2} l_{lm} l_{mk} s_{mk+lm} s_m & \frac{1}{2} l_{mk} l_{kl} s_{kl+mk} s_k & \frac{1}{2} l_{kl} l_{lm} s_{lm+kl} s_l \\ -l_{lm} l_{mk} c_{lm} c_{mk} s_m & -l_{mk} l_{kl} c_{mk} c_{kl} s_k & -l_{kl} l_{lm} c_{kl} c_{lm} s_l \end{bmatrix} \tag{A20}$$

and

$$\mathbf{B}_{klm} = \begin{bmatrix} -c_{kl} & -s_{kl} & c_{kl} & s_{kl} & 0 & 0 \\ 0 & 0 & -c_{lm} & -s_{lm} & c_{lm} & s_{lm} \\ c_{mk} & s_{mk} & 0 & 0 & -c_{mk} & -s_{mk} \end{bmatrix} \tag{A21}$$

with

$$s_i = \sin\theta_i \quad (i = k, l, m), \tag{A22}$$

$$c_{ij} = \cos\theta_{ij}, \quad s_{ij} = \sin\theta_{ij} \quad (ij = kl, lm, mk), \tag{A23}$$

and

$$s_{ij+pq} = s_{ij} c_{pq} + c_{ij} s_{pq} \quad (ij = kl, lm, mk; pq = mk, kl, lm). \tag{A24}$$

Here, θ_{ij} denotes the angle between a side $\overline{P_i P_j}$ and the x_1-axis, and θ_i the internal angle at a vertex P_i $(i = k, l, m)$ of the triangle $\Delta P_k P_l P_m$.